

Edge-controlled growth and kinetics of single-crystal graphene domains by chemical vapor deposition

Teng Ma^a, Wencai Ren^{a,1}, Xiuyun Zhang^b, Zhibo Liu^a, Yang Gao^a, Li-Chang Yin^a, Xiu-Liang Ma^a, Feng Ding^{b,c,1}, and Hui-Ming Cheng^{a,1}

^aShenyang National Laboratory for Materials Science, Institute of Metal Research, Chinese Academy of Sciences, Shenyang 110016, People's Republic of China; ^bInstitute of Textiles and Clothing, Hong Kong Polytechnic University, Kowloon, Hong Kong, People's Republic of China; and ^cBeijing Computational Science Research Center, Hai-Dian District, Beijing 100084, People's Republic of China

Edited by Hongjie Dai, Stanford University, Stanford, CA, and accepted by the Editorial Board November 4, 2013 (received for review July 6, 2013)

The controlled growth of large-area, high-quality, single-crystal graphene is highly desired for applications in electronics and optoelectronics; however, the production of this material remains challenging because the atomistic mechanism that governs graphene growth is not well understood. The edges of graphene, which are the sites at which carbon accumulates in the two-dimensional honeycomb lattice, influence many properties, including the electronic properties and chemical reactivity of graphene, and they are expected to significantly influence its growth. We demonstrate the growth of single-crystal graphene domains with controlled edges that range from zigzag to armchair orientations via growth–etching–regrowth in a chemical vapor deposition process. We have observed that both the growth and the etching rates of a single-crystal graphene domain increase linearly with the slanted angle of its edges from 0° to ~19° and that the rates for an armchair edge are faster than those for a zigzag edge. Such edge-structure-dependent growth/etching kinetics of graphene can be well explained at the atomic level based on the concentrations of the kinks on various edges and allow the evolution and control of the edge and morphology in single-crystal graphene following the classical kinetic Wulff construction theory. Using these findings, we propose several strategies for the fabrication of wafer-sized, high-quality, single-crystal graphene.

two-dimensional materials | crystal growth

Graphene, a one-atom-thick, two-dimensional (2D) crystal, has attracted increasing interest because of its interesting properties, which include a large carrier mobility, high transparency, extremely high thermal conductivity, and high tensile strength (1–3). Wafer-sized single-crystal graphene is highly desired and required for numerous applications, especially in electronics and optoelectronics, because grain boundaries between the graphene domains markedly degrade its quality and properties (4–8). Chemical vapor deposition (CVD) has shown great potential for growing large-sized single-crystal graphene domains (8–12); however, the growth rate with CVD is low, typically less than 20 μm/min, which is obviously not conducive to the fabrication of wafer-sized single crystals. In addition, the graphene produced by CVD suffers from poor controllability and low quality. For example, only zigzag (ZZ) or randomly oriented edges have been fabricated via CVD, and the electron mobility in CVD-produced graphene is substantially lower than that in mechanically exfoliated graphene (13). Understanding the atomistic mechanism that governs graphene growth is necessary for the controlled growth of wafer-sized, high-quality, single-crystal graphene. The edge structure of graphene has been shown to significantly influence its various fundamental properties, such as its electronic and magnetic properties, its edge stability, and its chemical reactivity (14–18). Similarly, the graphene edges, as the sites at which carbon accretion to the two-dimensional honeycomb lattice occurs, likely influence the graphene growth (19–21).

We report the growth of single-crystal graphene domains with controlled edges with orientations that range from ZZ to armchair (AC) via a CVD growth–etching–regrowth (G–E–RG) process. We observed that both the graphene growth and etching via CVD are strongly dependent on the edge structure. Such growth/etching behavior is well explained at the atomic level given the concentrations of kinks on the various edges and allows the evolution and control of the graphene edges and the morphology according to the classical kinetic Wulff construction (KWC) theory. Thus, we explain the commonly observed ZZ edges and low graphene growth rate under CVD and propose several strategies for the fabrication of wafer-sized, high-quality, single-crystal graphene.

Results

Morphology, Edge Evolution, and Control over Single-Crystal Graphene in CVD. We used ambient CVD with a platinum foil substrate to investigate the morphology evolution and to tune the edge structure of single-crystal graphene domains. In a typical G–E–RG process, only the methane flow rate was changed to induce the growth, etching, and regrowth of the graphene; all other parameters were held constant (*SI Appendix*, Fig. S1). The experiments were highly reproducible, and most of the graphene domains obtained over a given reaction time exhibited similar structures (*SI Appendix*, Figs. S2 and S3). The morphology of the graphene domains on Pt was characterized by scanning electron microscopy (SEM), and the edge structure of the graphene domains

Significance

Controlled synthesis of wafer-sized single crystalline high-quality graphene is a great challenge of graphene growth by chemical vapor deposition because of the complicated kinetics at edges that govern the growth process. Here we report the synthesis of single-crystal graphene domains with tunable edges from zigzag to armchair via a growth–etching–regrowth process. Both growth and etching of graphene are strongly dependent on the edge structure. This growth/etching behavior is well explained at the atomic level, given the concentrations of kinks on various edges, and allows control of graphene edges and morphology according to the classical kinetic Wulff construction theory. This work provides a deep understanding of the fundamental problems that limit graphene growth by chemical vapor deposition.

Author contributions: W.R. and H.-M.C. designed research; T.M., W.R., X.Z., and F.D. performed research; Z.L. and X.-L.M. contributed new reagents/analytic tools; T.M., W.R., X.Z., Z.L., Y.G., L.-C.Y., F.D., and H.-M.C. analyzed data; and T.M., W.R., F.D., and H.-M.C. wrote the paper.

The authors declare no conflict of interest.

This article is a PNAS Direct Submission. H.D. is a guest editor invited by the Editorial Board.

¹To whom correspondence may be addressed. E-mail: wcren@imr.ac.cn, feng.ding@polyu.edu.hk, or cheng@imr.ac.cn.

This article contains supporting information online at www.pnas.org/lookup/suppl/doi:10.1073/pnas.1312802110/-DCSupplemental.

was identified via Raman spectroscopy, transmission electron microscopy (TEM), and selective area electron diffraction (SAED) after being transferred onto Si/SiO₂ (280 nm thick) substrate or a TEM grid, using a bubbling transfer method (*SI Appendix*, Tables S1 and S2 and Figs. S4–S12).

Fig. 1 shows the typical structure of single-crystal graphene domains obtained at various reaction times during a CVD G–E–RG process. Hexagonal, single-crystal graphene domains with ZZ edges were grown on the Pt surface with a relatively high methane flow rate [3.7 standard-state cubic centimeter per minute (sccm)] (Fig. 1A and *SI Appendix*, Figs. S4 and S5). As the reaction time was increased, the domain size increased, whereas the ZZ edge structure remained unchanged (Fig. 1B). Surprisingly, when we slightly reduced the methane flow rate from 3.7 sccm to 3.3 sccm, the graphene domains switched from growing to being etched. When the etching time was increased, the domain size decreased, and the morphology and edge structure changed (Fig. 1C–G). First, two new slanted edges gradually formed at each vertex of the ZZ-edged hexagonal domain (Fig. 1C and *SI Appendix*, Fig. S13). Then, 12 new slanted edges moved inward, toward the AC direction. Eventually, the ZZ edges disappeared, leaving a dodecagonal domain with 12 identical slanted edges (Fig. 1D and *SI Appendix*, Fig. S6). During further etching, these 12 slanted edges moved inward and gradually became armchair-like (Fig. 1E and *SI Appendix*, Fig. S7), eventually transforming into

slanted edges with an ~19° angle from the ZZ edge (Fig. 1F and *SI Appendix*, Figs. S8, S9, and S14). After that, the edge direction remained almost unchanged (Fig. 1G), although the graphene domain continuously shrank. Hereafter, we refer to this specific edge structure as S19. It is also found that the etching rate of the graphene domains increases with the flow rate ratio of H₂/CH₄ (*SI Appendix*, Figs. S2 and S15 and Table S3). Combined with the high catalytic ability of Pt for the dissociation of H₂ to form active atomic H, we suggest that the atomic H plays an important role in the etching of graphene domains in our system.

By simply increasing the methane flow rate from 3.3 sccm to 3.5 sccm, we apparently induced regrowth of the etched graphene domains (Fig. 1H–L). First, the 12 slanted outer edges of the dodecagonal domain change to alternating AC and ZZ edges (Fig. 1H). Then, the six AC edges gradually shorten, whereas the six ZZ edges become longer (Fig. 1I–K and *SI Appendix*, Figs. S10 and S11). Finally, the graphene domain is transformed into a hexagon with ZZ edges (Fig. 1L and *SI Appendix*, Fig. S12). The hexagonal domain grows continuously with increasing reaction time but without any change to its morphology or edge structure (*SI Appendix*, Fig. S16), which is the same as that observed in Fig. 1A and B.

In addition to the evolution of the outer edge structure, a perfect hexagonal hole in the ZZ edges appears at the center of the dodecagonal domain and quickly expands; however, the ZZ

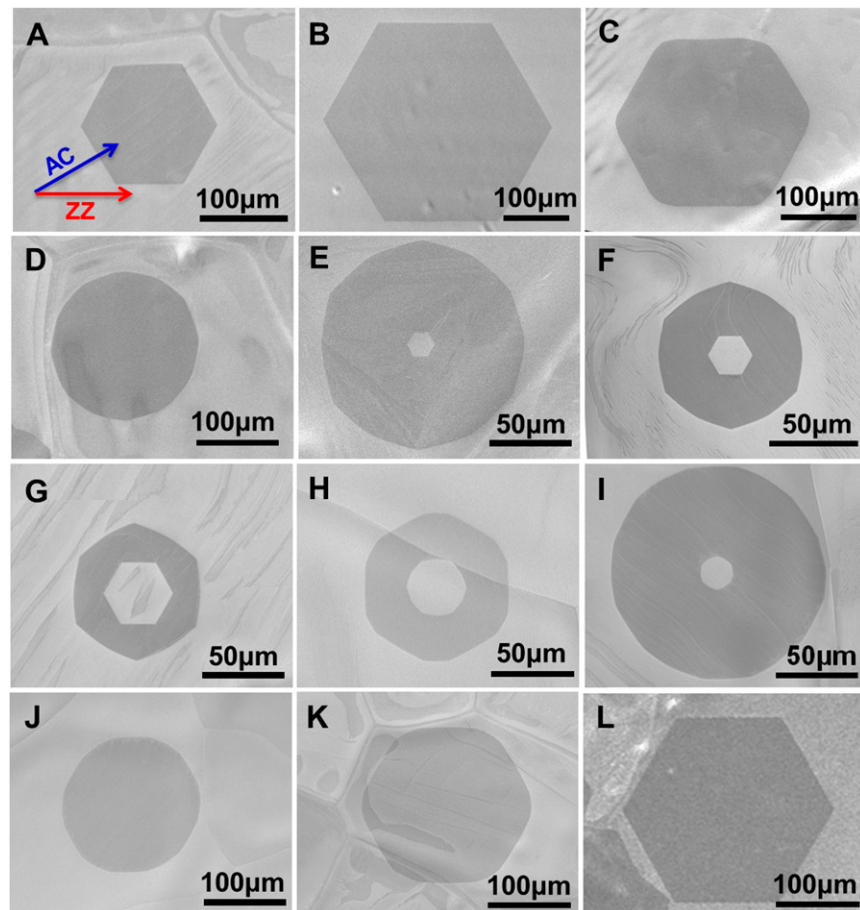


Fig. 1. Morphology and edge evolution of single-crystal graphene domains grown on a Pt surface during the G–E–RG process. (A and B) The growth stage: scanning electron microscopy (SEM) images of the hexagonal single-crystal graphene domain grown in a gas flow of 700 sccm hydrogen and 3.7 sccm methane with growth times of (A) 15 min and (B) 30 min. (C–G) The etching stage: SEM images depict a change in the single-crystal graphene domain with a gas flow of 700 sccm hydrogen and 3.3 sccm methane from B etched for (C) 4 min, (D) 7 min, (E) 10 min, (F) 11.5 min, and (G) 12 min. (H–L) The regrowth stage: SEM images of the single-crystal graphene domain regrown in a gas flow of 700 sccm hydrogen and 3.5 sccm methane from G with a regrowth time of (H) 0.5 min, (I) 2 min, (J) 3 min, (K) 5 min, and (L) 9 min. In all images, the ZZ edge of the graphene domain is oriented along the horizontal direction.

edge structure remains unchanged during the etching process (Fig. 1 E–G). The formation of the hole likely results from the structural defects formed during the graphene nucleation (22), and its unchanged edge directions, combined with the results of Raman spectroscopy analysis, provide strong evidence related to the crystallographic orientation of the outer edge. During the regrowth process, the inner hole shrinks and eventually disappears after its morphology evolves from a ZZ-edged hexagon (Fig. 1G) to a dodecagon with identical slanted edges (Fig. 1H) and then to a dodecagon with near-AC edges (Fig. 1I). This evolution is identical to that of the etching process at the outer edges of the hexagonal domains depicted in Fig. 1 C–G.

Edge-Structure-Dependent Growth and Etching of Single-Crystal Graphene. To achieve a quantitative understanding of the graphene growth and etching, we further studied the size evolution of the single-crystal graphene domains as a function of the reaction time during the etching and regrowth processes. Fig. 2A clearly demonstrates that the size evolution of the graphene domains as a function of time exhibits a nonlinear behavior. During the etching process, the shrinking of the single-crystal graphene domains accelerates. In contrast, the domains grow more and more slowly and eventually reach a constant growth rate after all of the edges have changed to ZZ during regrowth. A constant growth rate is also observed during the growth of the ZZ-edged hexagonal graphene domain (*SI Appendix*, Fig. S17). Because either the etching or the regrowth was performed under constant experimental conditions and was accompanied by a continuous edge evolution, the rates of both etching and regrowth must be edge-structure dependent. By fitting these data, we can obtain the etching and regrowth rates of a domain as a function of the average edge slanted angle, θ . The plots in Fig. 2B show a linear relationship between the etching/regrowth rate and θ ,

$$R_{E/G}(\theta) = R_{E/G0} + \beta_{E/G} \times \theta, \quad \text{for } 0 \leq \theta \leq 19^\circ, \quad [1]$$

where $R_{E/G0}$ is the etching/regrowth rate of the ZZ edge, and $\beta_{E/G}$ is a constant. Of the edges, the S19 exhibits the highest etching and regrowth rates, which are two and six times greater than that of the ZZ edge, respectively. Moreover, the AC edge grows faster than the ZZ edge (*SI Appendix*, Fig. S18).

Theoretical Calculation. During the growth/etching of a graphene domain, the kinetics are determined by the addition/removal of

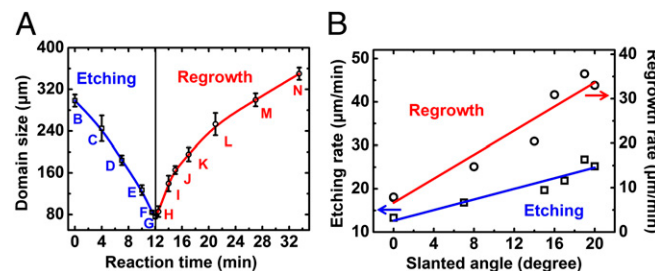


Fig. 2. Edge-structure-dependent growth/etching of single-crystal graphene domains. (A) Evolution of the size of single-crystal graphene domains as a function of the reaction time during etching and regrowth. The blue and red lines represent the fitting curves. Tens of graphene domains with the same structure were measured for each condition; the error bars indicate the variation in size. The typical graphene structure obtained at the measured reaction time (denoted with letters from B to N) is presented in Fig. 1 B–L and in *SI Appendix*, Fig. S16. (B) The rates of etching and regrowth of the graphene domains as functions of the average slanted angle θ . $\theta = \sum \theta_i / \sum l_i$, where θ_i is the slanted angle relative to the ZZ direction of an edge in a graphene domain, and l_i is the length of the corresponding edge. The red and blue lines represent the linear fits of the data.

carbon atoms onto/from the graphene edges. Both the AC and the ZZ edges are straight, with all edge carbon atoms located in a straight line. Therefore, the growth/etching of a straight AC/ZZ edge must be initiated by the formation of a nucleus or dent (Fig. 3 A and B). The height/depth of a nucleus/dent on a ZZ edge (h_{ZZ}) is 2.13 Å, whereas that on an AC edge (h_{AC}) is smaller at 1.23 Å. Therefore, the nucleus or dent on a ZZ edge may have higher formation energy than that on an AC edge. A slanted graphene edge can be considered as an AC or ZZ edge with kinks (Fig. 3 C–E). The addition or removal of carbon atoms onto/from a kink site leads to an only one-step propagation of the kink; any corresponding change in the formation energy should thus be negligible. Therefore, the kink sites are the most active for carbon addition or removal onto/from a graphene edge. If the graphene growth is attachment limited and all possibilities for carbon addition/removal onto/from an arbitrary graphene edge with a slanted angle θ are considered, then a simplified formula for the edge orientation-dependent growth/etching rate is (19, 21, 23, 24)

$$R(\theta) \approx n_{ZZ}(\theta) * \exp(-E_{ZZ}/kT) + n_{AC}(\theta) \exp(-E_{AC}/kT) + n_K(\theta), \quad [2]$$

where $n_{ZZ}(\theta)$, $n_{AC}(\theta)$, and $n_K(\theta)$ are the concentrations of the ZZ sites, the AC sites, and the kinks, respectively, along the edge.

The calculated formation energies of the ZZ and AC nuclei on a Pt(111) surface are 2.24 eV and 1.60 eV, respectively (Fig. 3F and *SI Appendix*), which is in agreement with the aforementioned analysis. Both of these energies are substantially greater than the thermal energy, $kT \approx 0.1$ eV, at the graphene growth temperature. Thus, the values of the first and second terms in Eq. 2 are substantially smaller than that of the third term unless $n_K(\theta) = 0$. Therefore, the growth/etching rate of a slanted edge is linearly proportional to the concentration of its kinks. As described in the literature (19, 20), the edge with a slanted angle of $\theta = 19.107^\circ$ has the largest kink concentration, and the kink concentration on the edges increases or decreases linearly with θ for θ in the range of 0° – 19.107° or 19.107° – 30° (*SI Appendix*, Fig. S19). Given Eq. 2, a linear relationship is expected between the growth/etching rate and θ for a slanted edge of $\theta = 19.107^\circ$ with the highest growth/etching rate of all edge types:

$$\begin{aligned} R(\theta) &\approx n_K(\theta) = \theta / h_{ZZ}, \quad \text{for } 0^\circ < \theta < 19.107^\circ \\ R(\theta) &\approx n_K(\theta) = (30^\circ - \theta) / h_{AC}, \quad \text{for } 19.107^\circ < \theta < 30^\circ. \end{aligned} \quad [3]$$

Given the larger barrier for initiating nucleation, the growth/etching rate of the ZZ edge must be slower than that of the AC edge. Therefore, the growth/etching rate of the graphene edges follows the order (23)

$$R_{S19} > R_{SL} > R_{AC} > R_{ZZ}, \quad [4]$$

where R_{S19} , R_{SL} , R_{AC} , and R_{ZZ} are the growth/etching rates of the S19, the other slanted, the AC, and the ZZ edges, respectively. These results are in perfect agreement with our experimental observations shown above.

Discussion

The aforementioned morphology evolution can be well explained by the classical theory of crystal growth (Fig. 3 G–I and *SI Appendix*, Figs. S20–S22). The morphology of a grown/etched crystal surface is governed by the dynamics of addition or removal of atoms, which is strongly dependent on the type of surface. However, in 2D graphene, the surface degenerates into linear edges. During the growth process, according to the KWC theory (25), the edges that grow rapidly become smaller; eventually, only the edges with the slowest growth rate (the ZZ edge) survive (Fig. 3 G and I). In contrast, during the etching process,

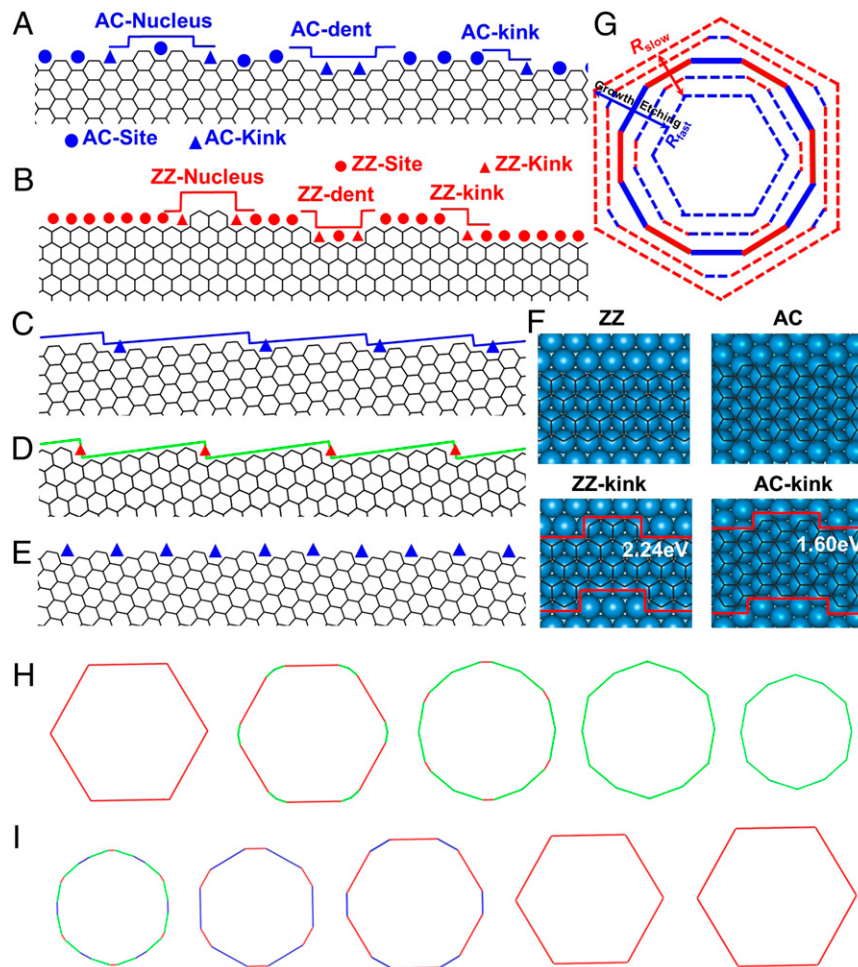


Fig. 3. Theoretical analyses of the growth and etching behaviors of single-crystal graphene domains. (A and B) Nucleus, dent, and kink formation on the (A) AC and (B) ZZ edges. (C and D) A slanted edge can be viewed as an AC or a ZZ edge with a series of kinks. (E) The slanted edge 19.1° from the ZZ direction exhibits the highest concentration of kinks (23). The kink sites and normal AC or ZZ sites are marked by the solid triangles and circles, respectively. (F) The models used to calculate the formation energies of the kinks on the ZZ and AC edges on the Pt(111) surface. For details of the calculation, see *SI Appendix*. (G) Illustration of the 2D KWC during crystal growth (indicated by the outward arrow) and etching (indicated by the inward arrow). The red and blue edges represent slower and faster growth/etching, respectively. (H and I) Illustrations of the edge and morphology evolution during (H) etching and (I) regrowth, as obtained by 2D KWC analyses (*SI Appendix*). The red, blue, and green lines represent the ZZ, AC, and S19 edges, respectively.

the edges with a slow etching rate disappear, and those with the highest etching rate (the S19 edges) eventually dominate the circumference of the graphene domain (Fig. 3 G and H). The growth/etching from the vertexes of a graphene domain leads to the formation of various edges, including ZZ, AC, and slanted edges ($\theta = 0^\circ$ to $\sim 19^\circ$). However, the evolution of the hole is opposite to that of the outer circumference of a 2D crystal because the hole-edge propagation during etching equals the growth of the outer circumference and vice versa. Therefore, the edge-structure-dependent growth/etching rate determines the edge and morphology evolution of the graphene domains during both CVD growth and etching processes.

These results indicate that graphene edges do not maintain a constant orientation during both CVD growth and etching and that the morphology of the graphene domains is not determined by nucleation; the morphology is rather determined by the dynamics of the addition/removal of carbon atoms onto/from their edges. Such unique growth/etching behavior of graphene differs noticeably from that of its one-dimensional counterpart, single-walled carbon nanotubes, whose chirality and growth rate remain unchanged over time under the same conditions because of their cylindrical topology (19, 23). This unique growth/etching behavior

of graphene allows us to tune the morphology and edge structure of single-crystal graphene domains by simply changing the reaction time and the flow rate of the carbon feedstock. Because the rapidly growing slanted edges disappear quickly, the growth of single-crystal graphene domains is largely governed by the addition of carbon atoms onto the surviving ZZ edges with the slowest growth rate. Thus, the observed average growth rate of single-crystal graphene domains is relatively low, especially over long reaction times (8–12). We suggest that an increase in the growth temperature and the use of substrates with low ZZ nucleus formation energies provide two possibilities for increasing the graphene growth rate because these approaches can potentially increase the addition rate of carbon atoms onto the ZZ edges. In our experiments, for example, the average growth rate of single-crystal graphene on Pt increased approximately twofold at the higher growth temperature of 1,070 °C, even at a low methane flow rate of 3.0 sccm. The average growth rate of single-crystal graphene on liquid Cu can reach 50 μm/min at 1,080–1,160 °C (26).

In addition, the regrown graphene domains are defect-free (*SI Appendix*, Fig. S12), which indicates the perfect incorporation of carbon atoms onto the domain edges. We further confirmed the high quality of the regrown graphene domains via etching (Fig. 4).

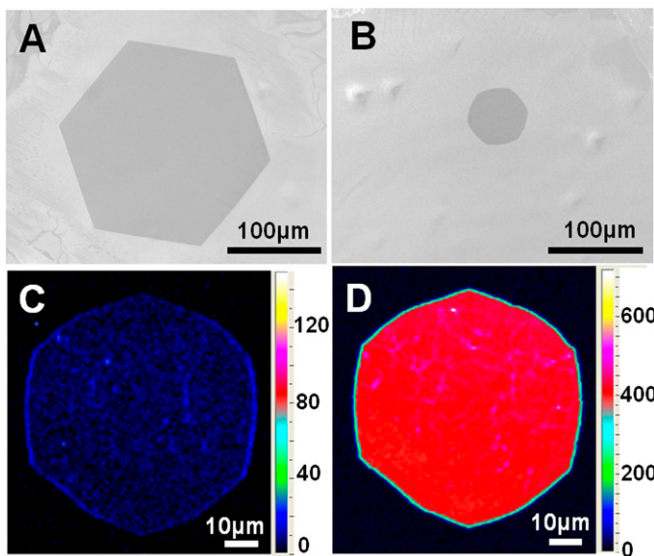


Fig. 4. Regrowth of defect-free single-crystal graphene domains. (A) SEM image of a regrown hexagonal single-crystal graphene domain in a gas flow of 700 sccm hydrogen and 3.5 sccm methane for 7 min from Fig. 1G. (B) SEM image of a near-hexagonal single-crystal graphene domain obtained by etching the regrown graphene domain in a gas flow of 700 sccm hydrogen and 3.3 sccm methane for 8 min from A. (C and D) D-peak (C) and G-peak (D) mapping of an etched, regrown graphene domain.

As shown in Fig. 1 E–G, a hole typically appears in the center of the as-grown single-crystal graphene domain after a given etching time because of the structural defects that form during graphene nucleation (22). In contrast, visible holes do not appear in the regrown graphene domains during etching even after their outer edges have transformed into S19 (Fig. 4B and *SI Appendix*, Fig. S23), and the Raman spectra of these domains do not show strong defect-related D peaks ($1,300\text{--}1,400\text{ cm}^{-1}$) (Fig. 4C); these results suggest a complete healing of the structural defects during regrowth. Therefore, the regrowth of graphene provides an effective method for healing defects and improving the quality of defective single-crystal graphene. In addition, the density of the graphene domains can be tuned via etching (*SI Appendix*, Fig. S23). We eventually obtained a single graphene domain by extending the etching time. Therefore, the observed high reversibility of the graphene etching and regrowth, combined with the varying activation energies for graphene nucleation and growth (27), enables the CVD fabrication of wafer-sized, high-quality single-crystal graphene.

Conclusions

We report an experimental and theoretical study of the growth kinetics of single-crystal graphene during a CVD growth–etching–regrowth process. We found that the graphene edges and morphologies are not determined by the nucleation but are kinetically

controlled during the CVD process and that defects in the graphene can be healed through an etching–regrowth process. We observed that the growth/etching rate of the graphene edges follows the order $R_{S19} > R_{SL} > R_{AC} > R_{ZZ}$ and increases linearly with the slanted angles within 0° – 19° relative to the ZZ direction. These results are explained theoretically at the atomic level by the different kink concentrations on various edges (23). Such edge-structure-dependent growth and etching behaviors combined with the KWC theory explain the edge and morphology evolution and the experimental observations that, with respect to the preparation of single-crystal graphene via the CVD process, the ZZ edge is dominant, and the graphene growth rate is low. This work provides a deeper understanding of the fundamental problems that limit the applications of CVD-grown graphene, and we have proposed several strategies for the fabrication of wafer-sized, high-quality, single-crystal graphene.

Methods

CVD Growth of Graphene. A typical G–E–RG experiment includes three stages: growth, etching, and regrowth (*SI Appendix*, Fig. S1). For graphene growth, a piece of Pt foil (180 μm thick, 99.9 wt% metal basis) was rinsed with acetone, water, and ethanol in sequence for 40 min each. The foil was then loaded into a fused-silica reaction tube (inner diameter: 22 mm) and heated to 1,040 °C under the protection of 200 sccm H₂; the Pt foil was annealed at 1,040 °C for 10 min in H₂ to remove any residual carbon or organic substances. Growth was then initiated and maintained for a certain time under a mixture of gaseous CH₄ (3.7 sccm) and H₂ (700 sccm). After the graphene growth stage, the CH₄ flow rate was reduced from 3.7 sccm to 3.3 sccm for graphene etching; the other parameters were held constant. After the graphene was etched, we regrew the graphene by increasing the CH₄ flow rate from 3.3 sccm to 3.5 sccm while holding all other parameters constant. The reaction time for each stage was recorded from the point at which the CH₄ flow rate was altered.

Characterization. To investigate the structure of the single-crystal graphene domains obtained after a given reaction time, the Pt foil was quickly removed from the high-temperature zone. The furnace was shut down, and the CH₄ flow was stopped after the furnace temperature decreased to less than 600 °C. Such operations ensure a rapid quenching of the reactions and allow the structure to be captured after a given time. Then, the Pt foil covered by the graphene domains was taken out for morphological analysis of the graphene via SEM (Nova NanoSEM 430, acceleration voltage of 15 kV). The graphene domains were then transferred onto a Si/SiO₂ (280 nm thick) substrate or a TEM grid, using a bubbling transfer method for optical (Nikon LV100D) and Raman analyses (JY HR800) or TEM (FEI Tecnai T12, 120 kV) observations and SAED measurements to identify their edge structures (*SI Appendix*). Because the bubbling transfer process does not cause any structural change in the Pt substrate (8), the same Pt substrate was reused in additional growth experiments after the graphene transfer.

Calculations. The formation energies of the ZZ and AC nuclei were calculated within the density functional theory framework, as implemented using the Vienna Ab initio simulation package (*SI Appendix*).

ACKNOWLEDGMENTS. This work was supported by the National Science Foundation of China (Grants 51325205, 51290273, 51172240, 51221264, and 50972147), the Ministry of Science and Technology of China (Grant 2012AA030303), and the Chinese Academy of Sciences (Grant KGZD-EW-303-1).

1. Novoselov KS, et al. (2004) Electric field effect in atomically thin carbon films. *Science* 306(5696):666–669.
2. Geim AK, Novoselov KS (2007) The rise of graphene. *Nat Mater* 6(3):183–191.
3. Geim AK (2009) Graphene: Status and prospects. *Science* 324(5934):1530–1534.
4. Yazyev OV, Louie SG (2010) Electronic transport in polycrystalline graphene. *Nat Mater* 9(10):806–809.
5. Huang PY, et al. (2011) Grains and grain boundaries in single-layer graphene atomic patchwork quilts. *Nature* 469(7330):389–392.
6. Yu Q, et al. (2011) Control and characterization of individual grains and grain boundaries in graphene grown by chemical vapour deposition. *Nat Mater* 10(6):443–449.
7. Wei Y, et al. (2012) The nature of strength enhancement and weakening by pentagon-heptagon defects in graphene. *Nat Mater* 11(9):759–763.
8. Gao L, et al. (2012) Repeated growth and bubbling transfer of graphene with millimetre-size single-crystal grains using platinum. *Nat Commun* 3:699.
9. Li X, et al. (2011) Large-area graphene single crystals grown by low-pressure chemical vapor deposition of methane on copper. *J Am Chem Soc* 133(9):2816–2819.
10. Wu TR, et al. (2013) Triggering the continuous growth of graphene toward millimeter-sized grains. *Adv Funct Mater* 23(2):198–203.
11. Yan Z, et al. (2012) Toward the synthesis of wafer-scale single-crystal graphene on copper foils. *ACS Nano* 6(10):9110–9117.
12. Chen S, et al. (2013) Millimeter-size single-crystal graphene by suppressing evaporative loss of Cu during low pressure chemical vapor deposition. *Adv Mater* 25(14):2062–2065.
13. Schwierz F (2010) Graphene transistors. *Nat Nanotechnol* 5(7):487–496.
14. Son YW, Cohen ML, Louie SG (2006) Half-metallic graphene nanoribbons. *Nature* 444(7117):347–349.
15. Nakada K, Fujita M, Dresselhaus G, Dresselhaus MS (1996) Edge state in graphene ribbons: Nanometer size effect and edge shape dependence. *Phys Rev B Condens Matter* 54(24):17954–17961.

16. Radovic LR, Bockrath B (2005) On the chemical nature of graphene edges: Origin of stability and potential for magnetism in carbon materials. *J Am Chem Soc* 127(16):5917–5927.
17. Girit CO, et al. (2009) Graphene at the edge: Stability and dynamics. *Science* 323(5922):1705–1708.
18. Jia X, et al. (2009) Controlled formation of sharp zigzag and armchair edges in graphitic nanoribbons. *Science* 323(5922):1701–1705.
19. Artyukhov VI, Liu Y, Yakobson BI (2012) Equilibrium at the edge and atomistic mechanisms of graphene growth. *Proc Natl Acad Sci USA* 109(38):15136–15140.
20. Liu YY, Dobrin斯基 A, Yakobson BI (2010) Graphene edge from armchair to zigzag: The origins of nanotube chirality? *Phys Rev Lett* 105(23):235502.
21. Shu H, Chen X, Tao X, Ding F (2012) Edge structural stability and kinetics of graphene chemical vapor deposition growth. *ACS Nano* 6(4):3243–3250.
22. Yuan Q, et al. (2012) Magic carbon clusters in the chemical vapor deposition growth of graphene. *J Am Chem Soc* 134(6):2970–2975.
23. Rao R, Liptak D, Cherukuri T, Yakobson BI, Maruyama B (2012) In situ evidence for chirality-dependent growth rates of individual carbon nanotubes. *Nat Mater* 11(3):213–216.
24. Ding F, Harutyunyan AR, Yakobson BI (2009) Dislocation theory of chirality-controlled nanotube growth. *Proc Natl Acad Sci USA* 106(8):2506–2509.
25. Sekerka RF (2005) Equilibrium and growth shapes of crystals: How do they differ and why should we care. *Cryst Res Technol* 40(4–5):291–306.
26. Geng D, et al. (2012) Uniform hexagonal graphene flakes and films grown on liquid copper surface. *Proc Natl Acad Sci USA* 109(21):7992–7996.
27. Kim H, et al. (2012) Activation energy paths for graphene nucleation and growth on Cu. *ACS Nano* 6(4):3614–3623.

Supporting Information Appendix for

Edge-Controlled Growth and Kinetics of Single-Crystal Graphene Domains by Chemical Vapor Deposition

Growth, etching and regrowth of single-crystal graphene domains

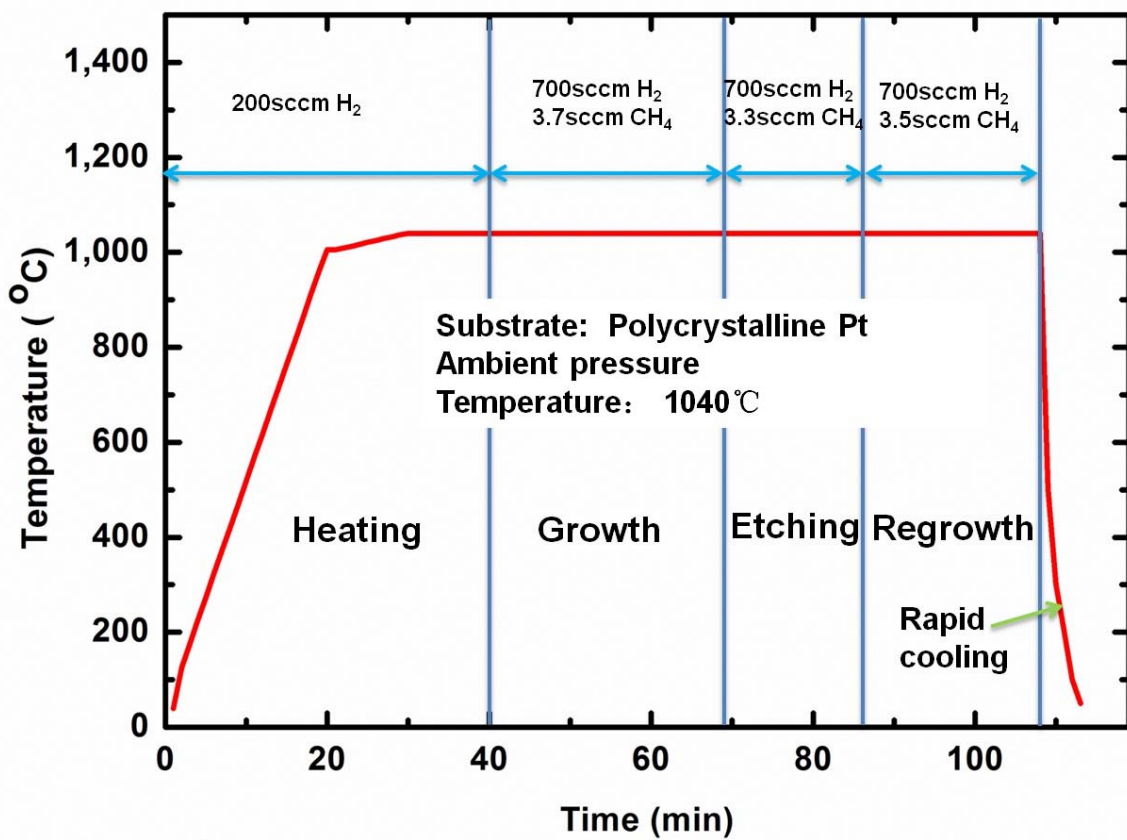


Fig. S1. Schematic of a typical CVD experiment process used for tuning the edge structure and investigating the structural evolution of single-crystal graphene domains.

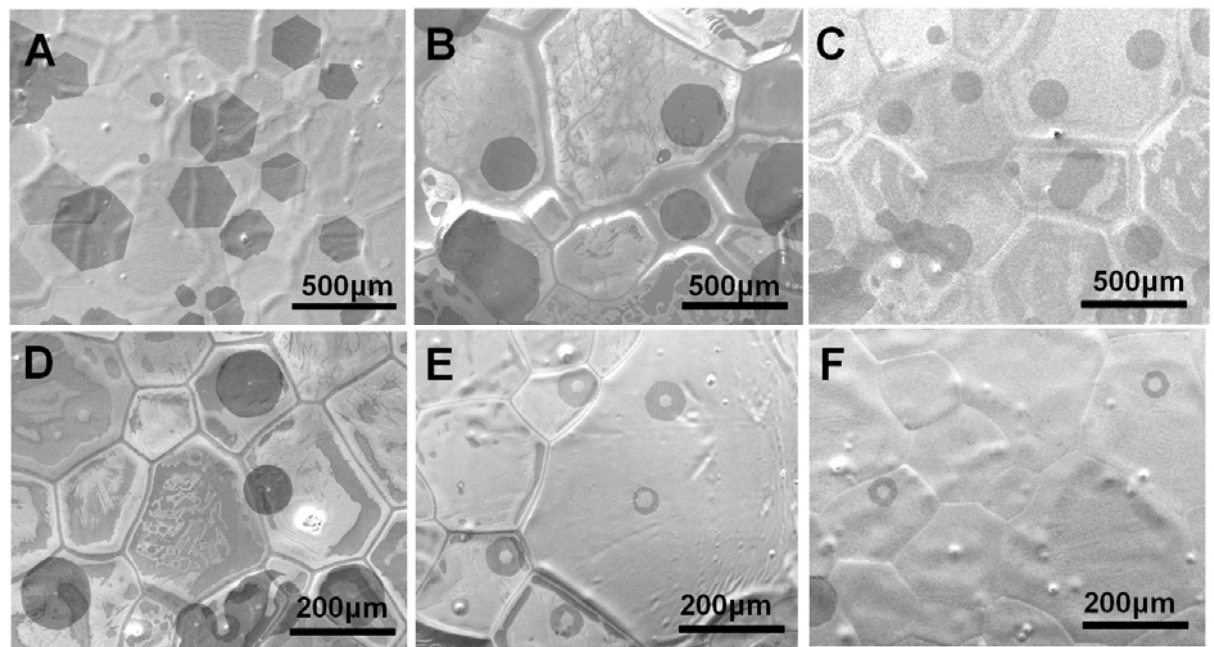


Fig. S2. Low-magnification SEM images of the graphene domains etched in a gas flow of 700 sccm hydrogen and 3.3 sccm methane from Fig. 1B in the main text for (A) 0, (B) 4, (C) 7, (D) 10, (E) 11.5, and (F) 12 min.

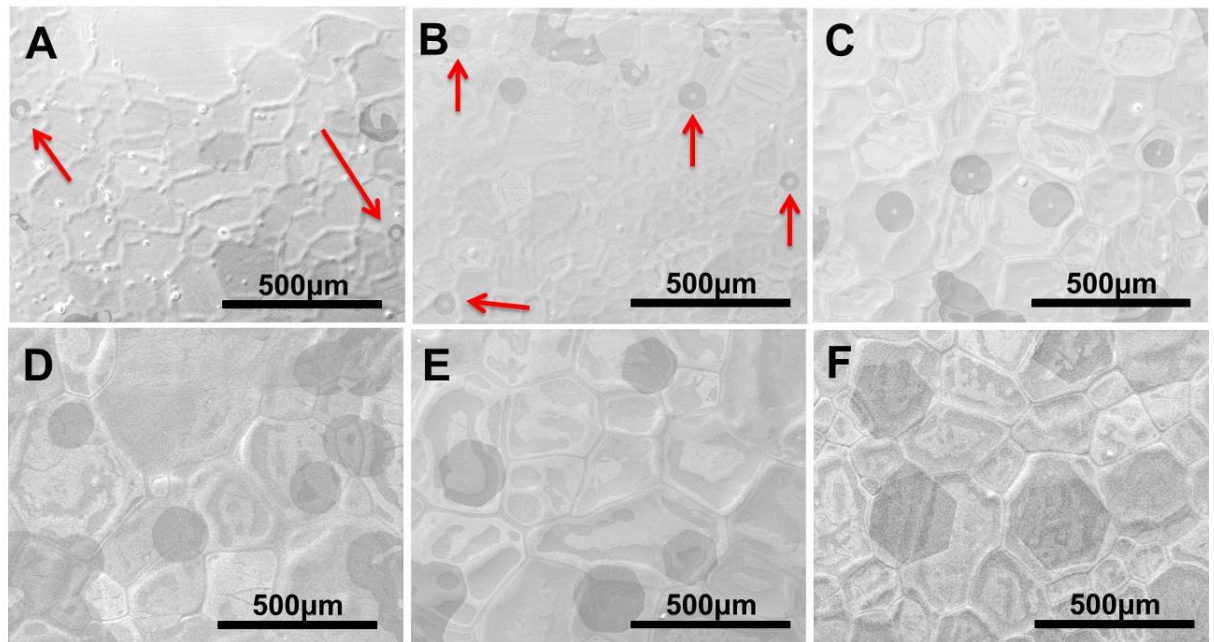


Fig. S3. Low-magnification SEM images of the regrown graphene domains obtained in a gas flow of 700 sccm hydrogen and 3.5 sccm methane from Fig. 1G in the main text with a regrowth time of (A) 0.5, (B) 1, (C) 2, (D) 3, (E) 5, and (F) 9 min.

Raman and TEM characterization of the single-crystal graphene structures

The Raman spectra of graphene were collected using a 532 nm laser under ambient condition with a JY HR800. The laser spot size was $\sim 1 \mu\text{m}$, and the laser power at the sample was below 2 mW to avoid laser heating induced sample damage. The Raman mapping was obtained by measuring the sample with a step of $0.5 \mu\text{m}$, and the integration time at each position was 1 s.

The different edges of graphene show a big difference in Raman spectra (1-5), which allows us to precisely identify the edge structure of the graphene domain. Here, we identified 6 typical graphene structures formed during the growth-etching-regrowth process, including a perfect hexagonal domain (Fig. 1A in the main text), a dodecagonal domain (Fig. 1D in the main text), a dodecagonal domain with a hexagonal hole in it (Fig. 1E and F in the main text), a regrown dodecagonal domain (Fig. 1J in the main text) and a regrown hexagonal domain (Fig. 1L in the main text) by using Raman spectroscopy (Figs. S4, S6-S8, S10, and S12). Optical measurements indicate that the smooth edges of graphene maintained after transfer, which ensures the structure identification by Raman spectroscopy. The D peak is due to the breathing modes of sp^2 rings and requires a defect for its activation. The D peak is suppressed for a perfect zigzag (ZZ) edge because the exchange momentum by scattering from the ZZ edge cannot connect the adjacent Dirac cones and therefore does not fulfill the double resonance process. In contrast, the exchange momentum from an armchair (AC) edge can satisfy the inter-valley scattering process, therefore, a strong D peak is usually observed in the AC edge (1). In addition, the G peak of ZZ and AC

edges responses differently to the polarization of the incident laser because the unequal interaction between the two degenerate components of the G peak, longitudinal optical and transverse optical phonons, with electrons at the different types of edges. The ZZ edge shows a minimum and maximum G peak when the polarization of the incident laser is parallel and perpendicular to the edge directions, respectively, and the AC edge shows an opposite response (2).

Here, we identified the edge structure of single-crystal graphene domains through combined analyses on both the D peak and G peak behavior. In order to avoid the effect of laser polarization on the D peak intensity and to maximize the D peak intensity, the polarization of the incident laser was tuned to parallel to the edge direction during the D peak measurements. To define the exact edge position, we first collected the Raman spectra inside the domain, and then moved the laser spot very carefully with a step of 100 nm to the edges until the G peak intensity (I_G) was half of that inside the domain (3, 4). For polarized G peak measurements, the polarization of the incident laser was tuned by rotating a half-wave plate, and the angle of the laser polarization relative to the edge direction was defined as α .

In addition, we also used TEM and SAED to directly identify the edge structure of the single-crystal graphene domains. Three typical graphene structures obtained during the growth-etching-regrowth process were measured, including a perfect hexagonal domain (Fig. 1A in the main text), a dodecagonal domain with a hexagonal hole in it (Fig. 1F in the main text), and a regrown dodecagonal domain (Fig. 1J in the main text). The TEM images and the corresponding SAED patterns of different graphene structures are shown in Figs. S5, S9 and S11. It is worth noting that all the measured areas in a grain show the same electron diffraction patterns, confirming their single crystal nature. As reported before (6), the crystal direction of a

grain's edges was determined by comparing the orientation of the grain in real space with the orientation of the corresponding diffraction pattern, and the characterization results are shown in Table S2. These characterization results are in good agreement with those obtained by Raman analysis.

Table S1 Raman characterization of the edges of various single-crystal graphene domains

Representative structure	Fig. 1A	Fig. 1D	Fig. 1E	Fig. 1E	Fig. 1F	Fig. 1F	Fig. 1J	Fig. 1L
Raman spectra	Fig. S4	Fig. S6	Fig. S7	Fig. S7	Fig. S8	Fig. S8	Fig. S10	Fig. S12
Domain Shape	Hexagon	Dodecagon	Hexagonal hole	Dodecagonal outer edge	Hexagonal hole	Dodecagonal outer edge	Dodecagon	Hexagon
I_D/I_G	2.5%	4.5%	4.9%	5.2%	5.2%	11.5%	Neighboring edges: 9.5%, 4.7%	2.8%
$I_G \sim \alpha$	↑	-	↑	↓	↑	↓	Neighboring edges: ↓, ↑	↑
Edge structure	ZZ	Mixed	ZZ	Near AC	ZZ	Near AC	AC, ZZ	ZZ

Table S2 Characterization of the edges of three typical single-crystal graphene domains by using TEM and SAED.

Representative structure	Fig. 1A	Fig. 1F	Fig. 1F	Fig. 1J
TEM image and SAED pattern	Fig. S5	Fig. S9	Fig. S9	Fig. S11
Domain Shape	Hexagon	Hexagonal hole	Dodecagonal outer edge	Dodecagon
Angle between ZZ direction determined by SAED and the edge direction in real space	0°	0°	19°	30°, 0°
Edge structure	ZZ	ZZ	Near AC	AC, ZZ

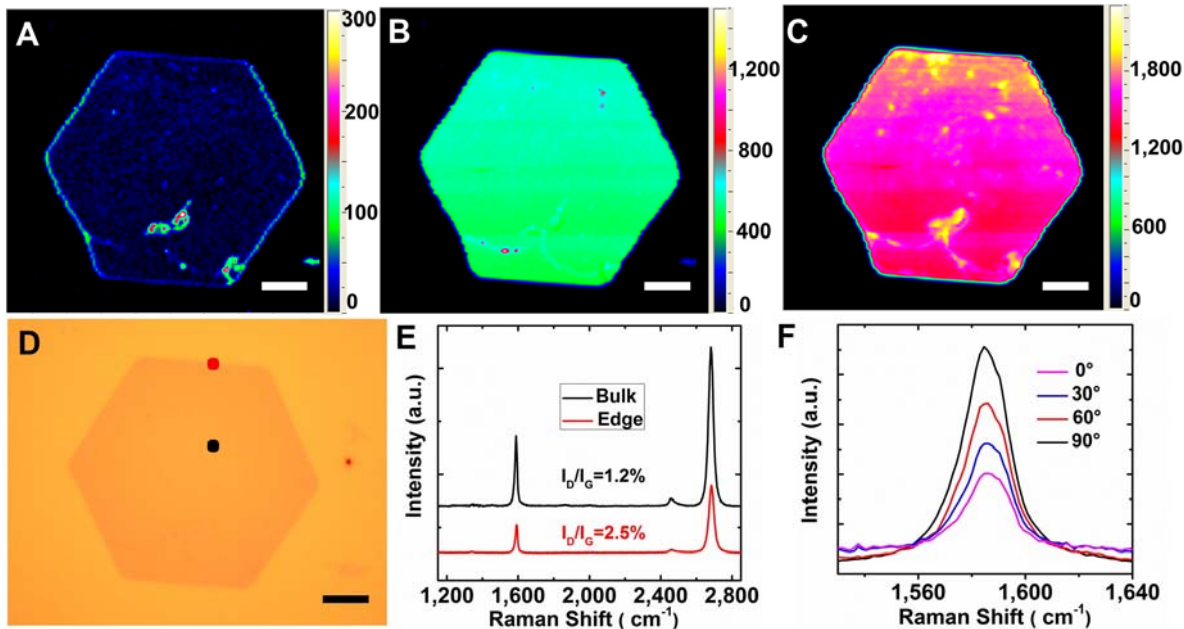


Fig. S4. (A) D-peak, (B) G-peak, and (C) 2D-peak intensity mappings and (D) the corresponding optical image of a hexagonal graphene domain, which was prepared with the same experimental condition as that shown in Fig. 1A in the main text. (E) A typical Raman spectrum and (F) polarization dependence of the G peak of the edges of the hexagonal graphene domain. For comparison, the Raman spectrum of a region inside the domain is also shown in E. All the scale bars are 20 μm . The polarization of the incident laser is along the vertical direction. Note that the edges show a relatively low D peak intensity, with an intensity ratio of D peak to G peak (I_D/I_G) of 2.5%, and their G-peak intensity increases with α , which indicates that the edges have a ZZ direction.

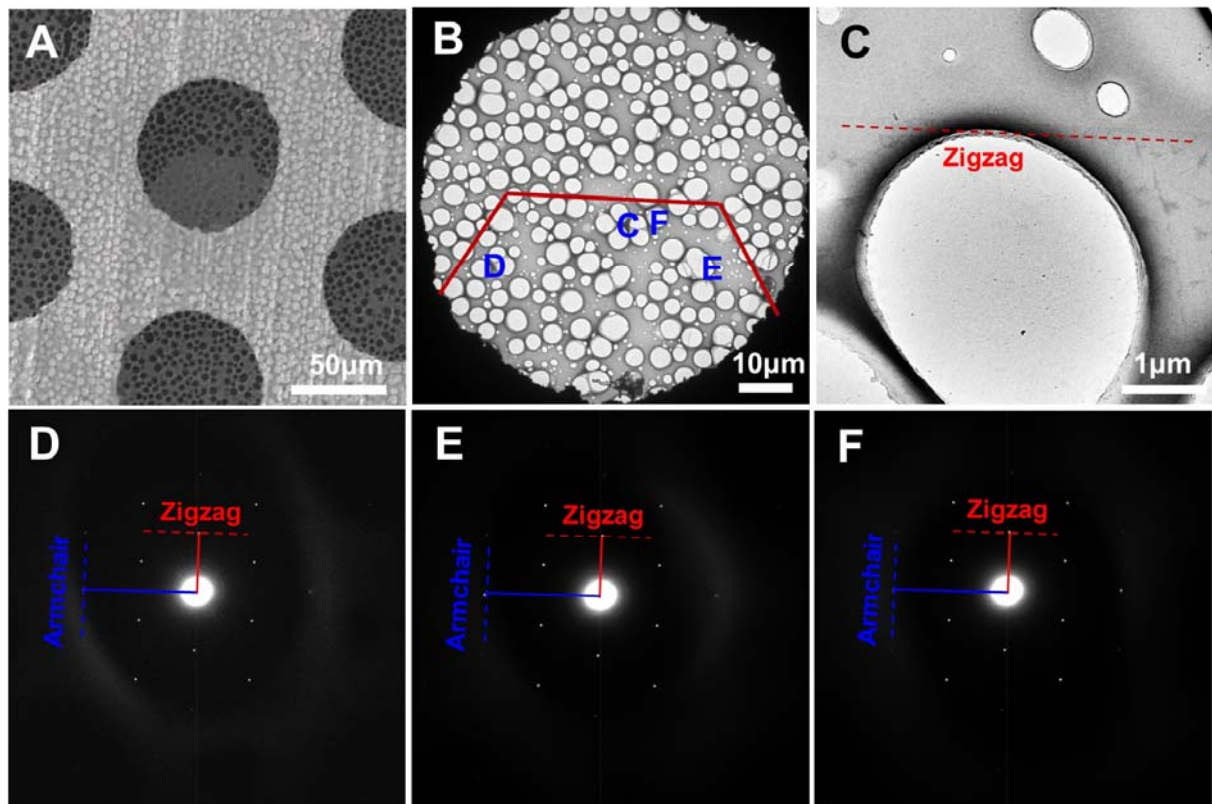


Fig. S5. (A) SEM image of a hexagonal graphene domain on a TEM grid, which was prepared with the same experimental condition as that shown in Fig. 1A in the main text. (B) Low-magnification TEM image of the graphene domain. The red lines indicate the graphene edges. (C) High-magnification TEM image of an edge of the hexagonal graphene domain in B. (D-F) SAED patterns taken from the suspended graphene areas in the holes of the TEM grid, which are indicated by D, E, and F in B. Red and blue dot lines indicate the ZZ and AC directions determined by SAED, respectively. Note that the angle between the ZZ direction determined by SAED and the edge direction in real space is 0° , suggesting the edge is ZZ type.

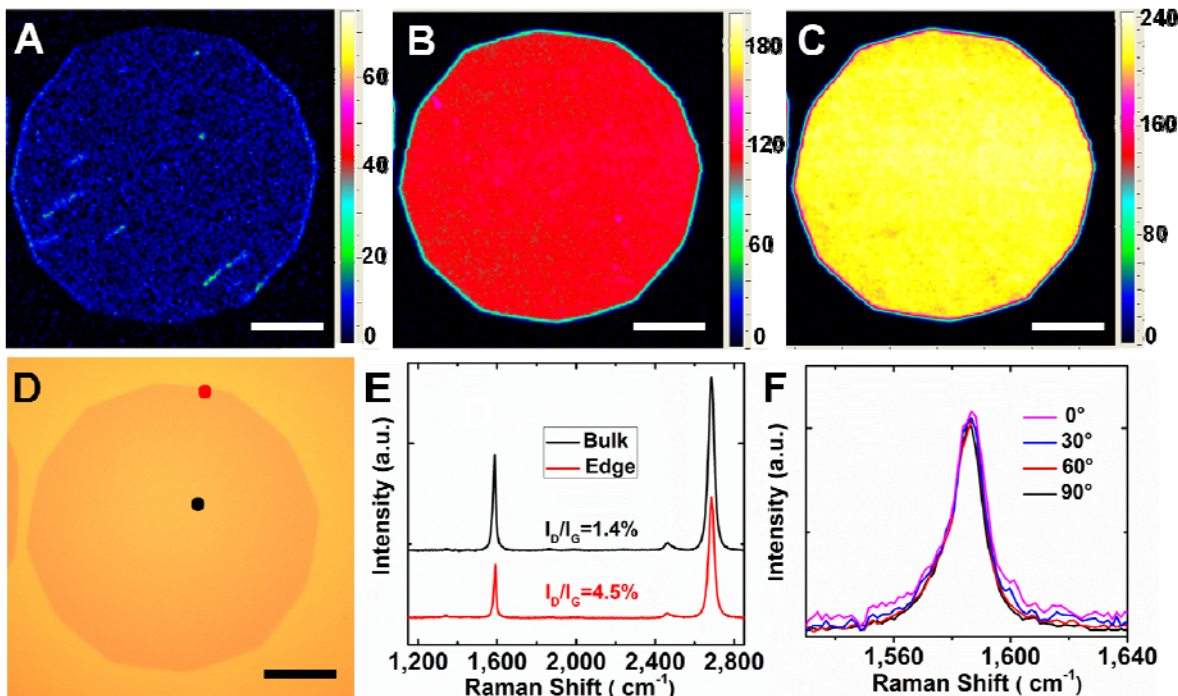


Fig. S6. (A) D-peak, (B) G-peak, and (C) 2D-peak intensity mappings and (D) the corresponding optical image of a dodecagonal graphene domain, which was etched in a gas flow of 700 sccm hydrogen and 3.3 sccm methane for 1 min from Fig. 1A in the main text. (E) A typical Raman spectrum and (F) polarization dependence of the G-peak of the edges of the dodecagonal graphene domain. For comparison, the Raman spectrum of a region inside the domain is also shown in E. All the scale bars are 20 μm . The polarization of the incident laser is along the vertical direction. Note that the edges at the same polarization conditions show almost the same D peak intensity, and the G-peak intensity is constant with α . Combined with the regular dodecagonal shape, we suggest that the dodecagonal domains have a mixed edge structure of ZZ and AC segments ($\sim 15^\circ$ relative to the ZZ direction), which is also consistent with the higher I_D/I_G compared to the ZZ edges shown in Fig. S4.

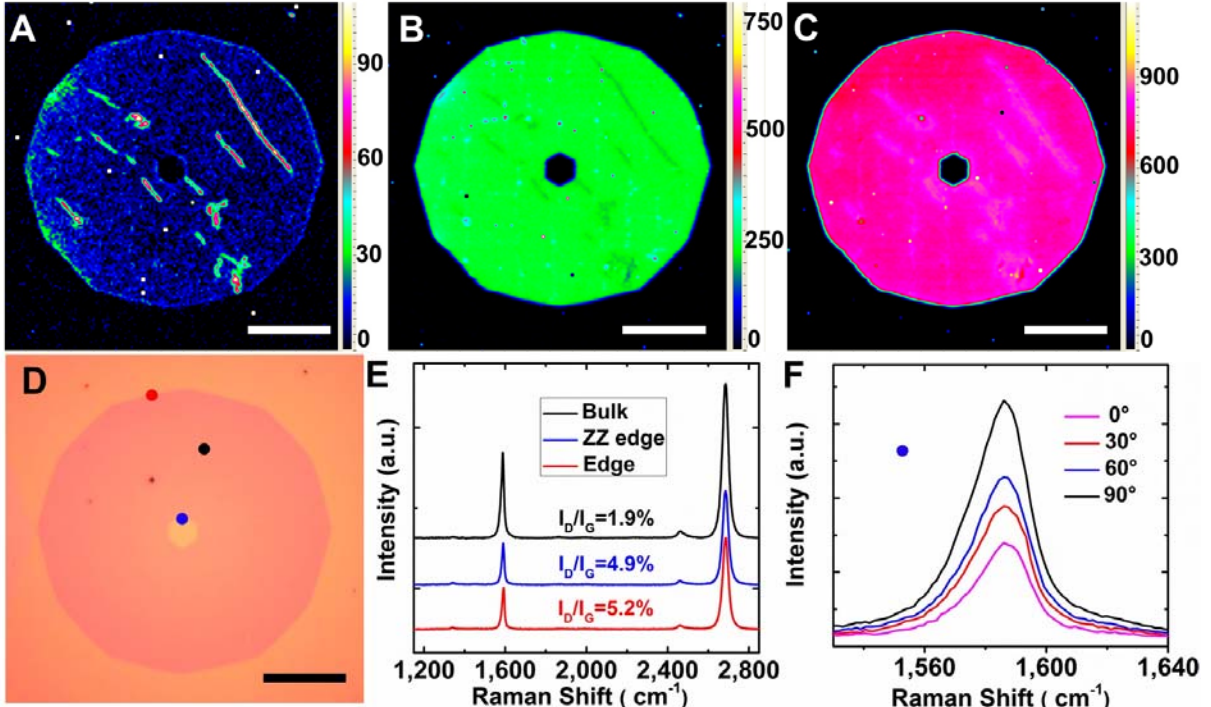


Fig. S7. (A) D-peak, (B) G-peak, and (C) 2D-peak intensity mappings and (D) the corresponding optical image of a dodecagonal graphene domain with a hexagonal hole in its center, which was etched in a gas flow of 700 sccm hydrogen and 3.3 sccm methane for 1.5 min from Fig. 1A in the main text. (E) A typical Raman spectrum and (F) polarization dependence of the G-peak of the edges of the hexagonal hole. For comparison, the Raman spectra of an outer edge and a region inside the domain are also shown in E. All the scale bars are 20 μm . The polarization of the incident laser used for Raman mapping measurements is circular, while that for G-peak polarization measurements is along the vertical direction. Note that the G-peak intensity of the edges of the hexagonal inner hole increases with α , which indicates that the edges have a ZZ direction. The higher I_D/I_G and the orientation relative to the ZZ direction suggest that the outer

edges have a mixed edge structure of ZZ and AC segments, similar to those shown in Fig. S6.

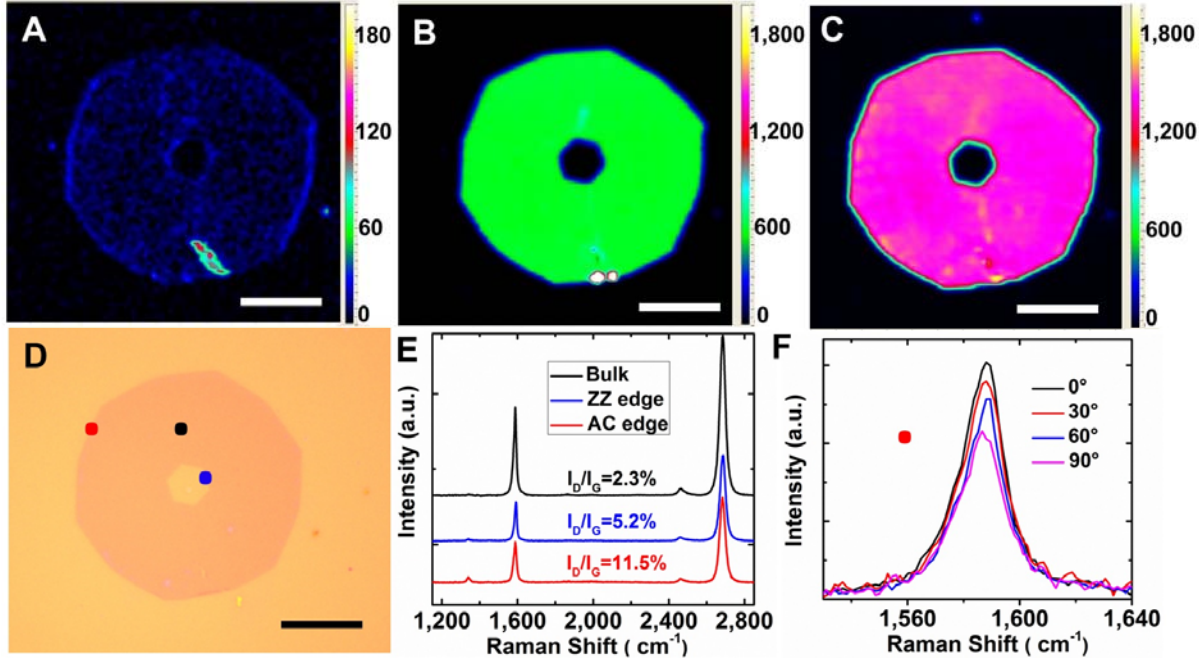


Fig. S8. (A) D-peak, (B) G-peak, and (C) 2D-peak intensity mappings and (D) the corresponding optical image of a dodecagonal graphene domain with a hexagonal hole in its center, which was etched in a gas flow of 700 sccm hydrogen and 3.3 sccm methane for 2 min from Fig. 1A in the main text. (E) A typical Raman spectrum and (F) polarization dependence of the G-peak of the outer edges of the dodecagonal domain. For comparison, the Raman spectra of an edge of the inner hole and a region inside the domain are also shown in E. All the scale bars are 20 μm . The polarization of the incident laser used for Raman mapping measurements is circular, while that for G-peak polarization measurements is along the vertical direction. Note that the outer edges show a very high I_D/I_G and their G-peak intensity decreases with α , which indicates that the outer edges have a near AC direction. The precise measurements on the angles between the outer

edges and the ZZ edges of the inner hole confirm that the outer edges have a direction of $\sim 19^\circ$ relative to the ZZ orientation.

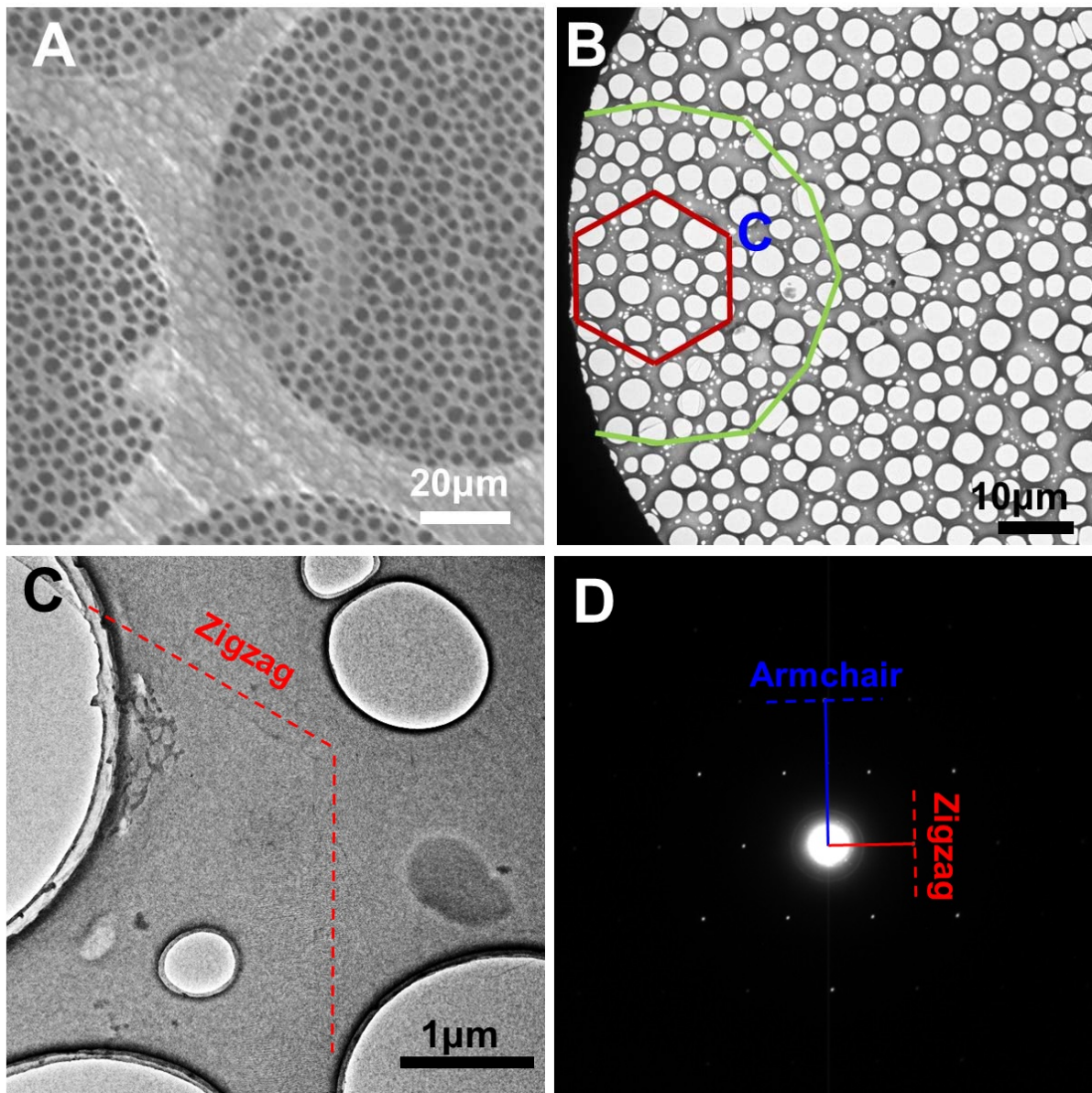


Fig. S9. (A) SEM image of a dodecagonal domain with a hexagonal hole on a TEM grid, which was prepared with the same experimental condition as that shown in Fig. S8. (B) Low-magnification TEM image of the graphene domain. The red and green lines indicate the edges of the hexagonal inner hole and the dodecagonal outer edges, respectively. (C)

High-magnification TEM image of two neighboring edges of the hexagonal hole. (D) SAED pattern taken from the suspended graphene area indicated by C in B. Red and blue dot lines indicate the zigzag and armchair directions determined by SAED, respectively. Note that the angle between the ZZ direction determined by SAED and the edge direction of the inner hole in real space is 0° , suggesting the edge is ZZ type. The dodecagonal outer edges are measured to be $\sim 19^\circ$ away from the ZZ direction.

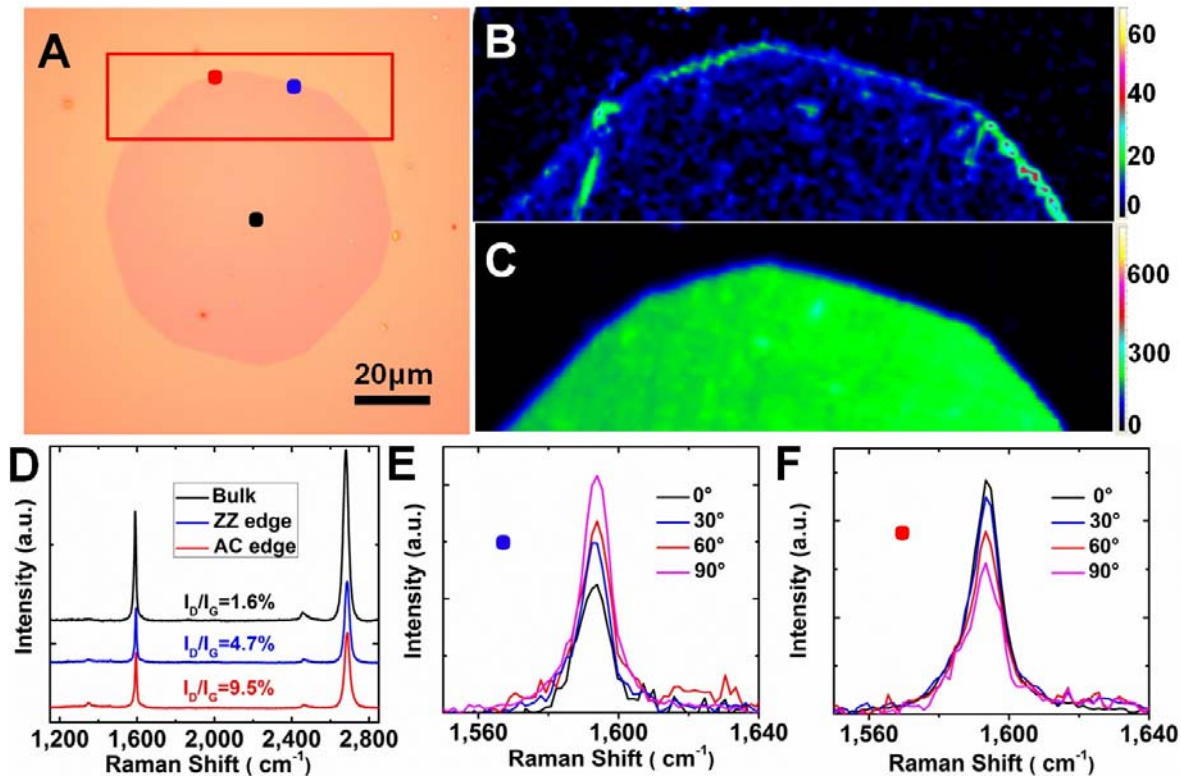


Fig. S10. (A) Optical image of a regrown dodecagonal graphene domain, which was regrown in a gas flow of 700 sccm hydrogen and 3.5 sccm methane for 0.5 min from Fig. S8. (B) D-peak and (C) G-peak intensity mappings of the region denoted with a rectangle box in A. (D–F) The typical Raman spectra and the polarization dependence of the G peaks of two neighboring edges

of the dodecagonal graphene domain. For comparison, the Raman spectrum of a region inside the domain is also shown in D. The polarized G-peak spectra shown in E and F were collected from the edges denoted by blue and red dots, respectively. The polarization of the incident laser used for Raman mapping measurements is circular, while that for G-peak polarization measurements is along the vertical direction. Note that the neighboring edges show opposite G-peak polarization dependence on α . Combining with the structural evolution from Fig. 1G, the ZZ direction of the edges of the inner hole shown in Fig. 1G and the relative orientation between the neighboring edges, we suggest that the regrown dodecagonal graphene domain have alternating AC (for example, the edge indicated by red dot in A) and ZZ (for example, the edge indicated by blue dot in A) edges. These results are consistent with the alternating D-peak intensity change for the neighboring edges under the circle polarization condition as shown in B.

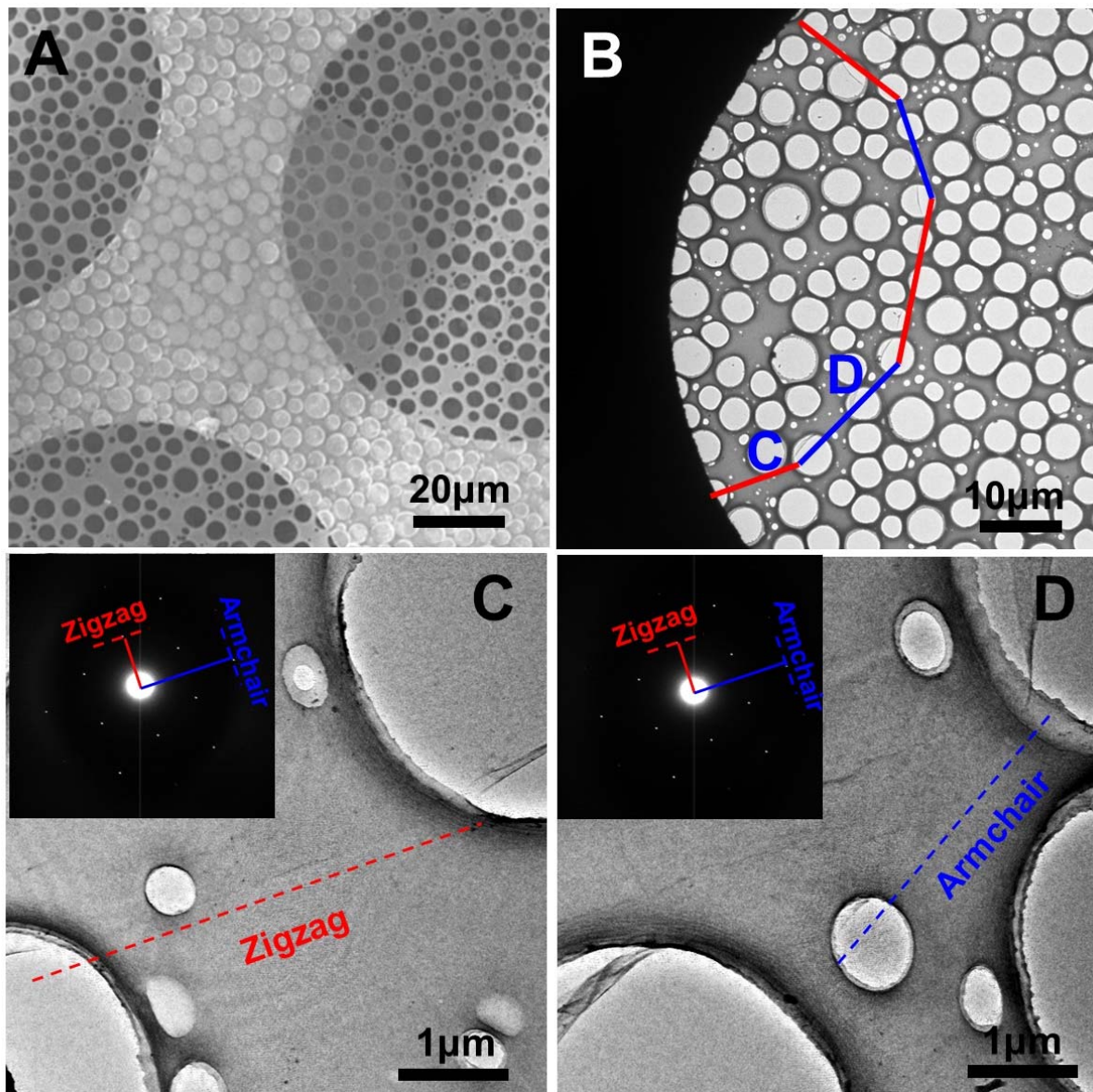


Fig. S11. (A) SEM image of a regrown dodecagonal domain on a TEM grid, which was prepared with the same experimental condition as that shown in Fig. S10. (B) Low-magnification TEM image of the graphene domain. The angle between neighboring edges (indicated by red and blue lines) is $\sim 150^\circ$. (C) High-magnification TEM image of the edge close to the suspended area indicated by C in B. Inset: SAED pattern taken from the suspended graphene area indicated by C in B. According to the ZZ (red dot line in Inset) and AC (blue dot line in Inset) directions

determined by SAED, this edge has a ZZ direction. (D) High-magnification TEM image of the edge close to the suspended graphene area indicated by D in B. Inset: SAED pattern taken from the suspended area indicated by D in B. According to the ZZ (red dot line in Inset) and AC (blue dot line in Inset) directions determined by SAED, this edge has an AC direction.

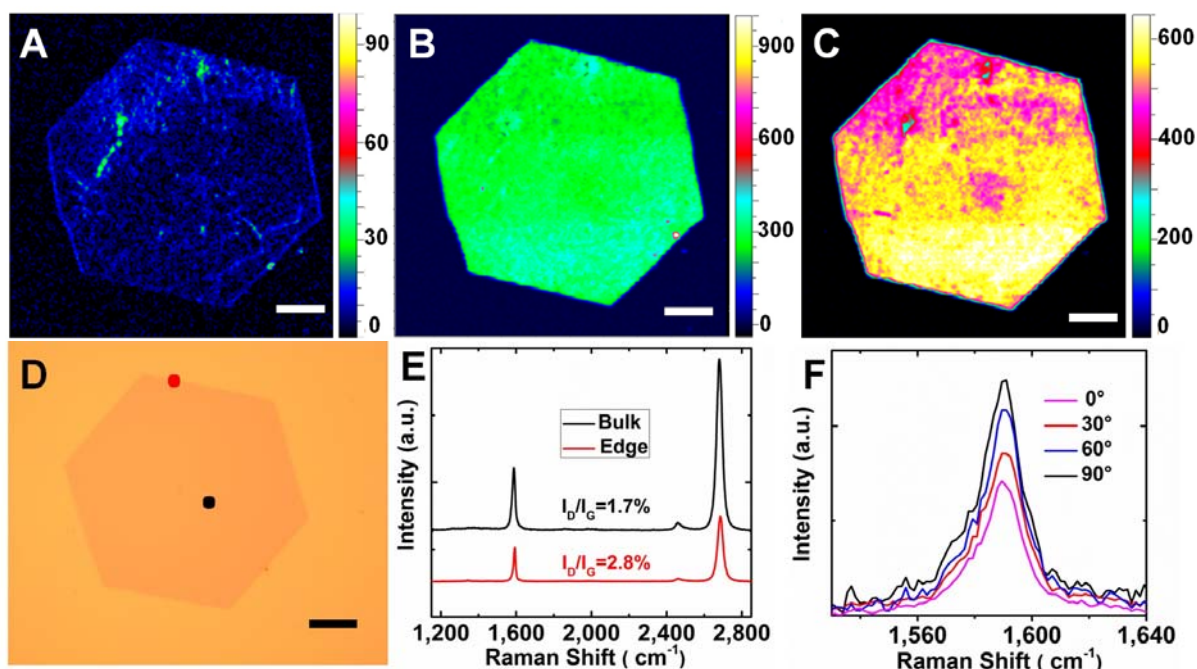


Fig. S12. (A) D-peak, (B) G-peak, and (C) 2D-peak intensity mappings and (D) the corresponding optical image of a regrown hexagonal graphene domain, which was regrown in a gas flow of 700 sccm hydrogen and 3.5 sccm methane for 2 min from Fig. S8. (E) A typical Raman spectrum and (F) polarization dependence of the G peak of the edges of the hexagonal graphene domain. For comparison, the Raman spectrum of a region inside the domain is also shown in E. All the scale bars are 20 μm . The polarization of the incident laser is along the vertical direction. Note that the edges show a relatively low D peak, with I_D/I_G of 2.8%, and their

G-peak intensity increases with α , which indicates that the edges have a ZZ direction. The very low D peak shown in A indicates that the regrown graphene domain is defect free, suggesting the perfect incorporation of carbon atoms onto the domain edges.

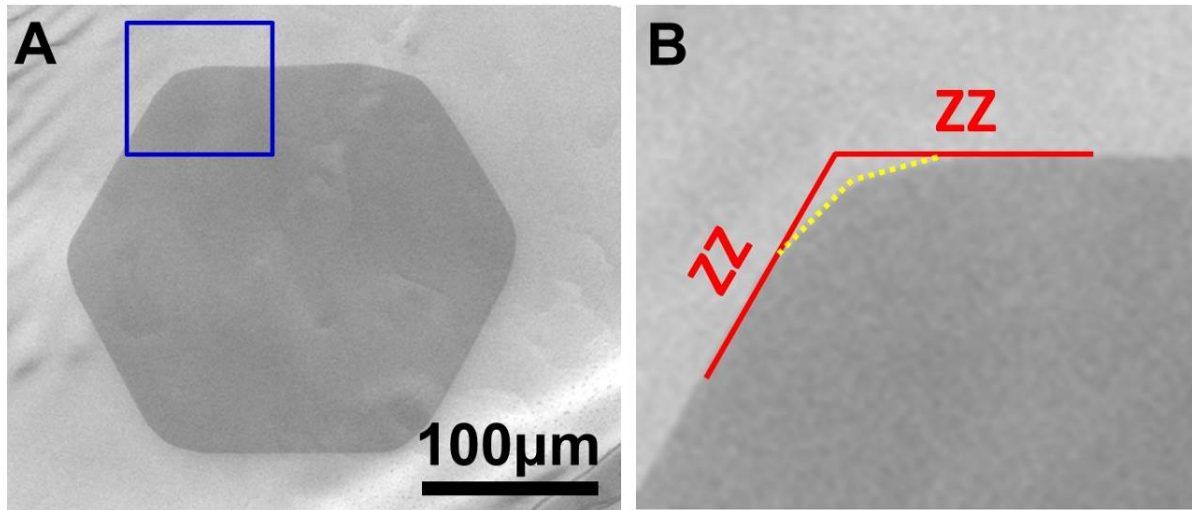


Fig. S13. (A) The graphene domain shown in Fig. 1C in the main text. (B) High-magnification SEM image of the region indicated by a square box in A. It is worth noting that two new short slanted edges (indicated by the yellow dot lines) which are slightly ($\sim 14^\circ$) deviated from the ZZ direction are formed at each vertex of the ZZ-edged hexagonal domain.

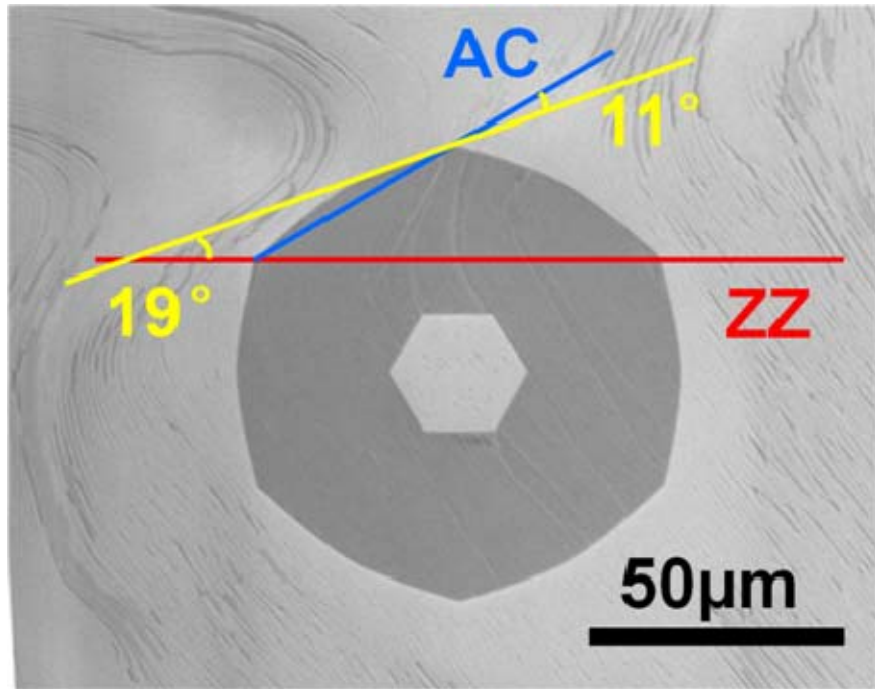


Fig. S14. The graphene domain shown in Fig. 1F in the main text. Note that the outer slanted edges are $\sim 19^\circ$ away from the ZZ direction.

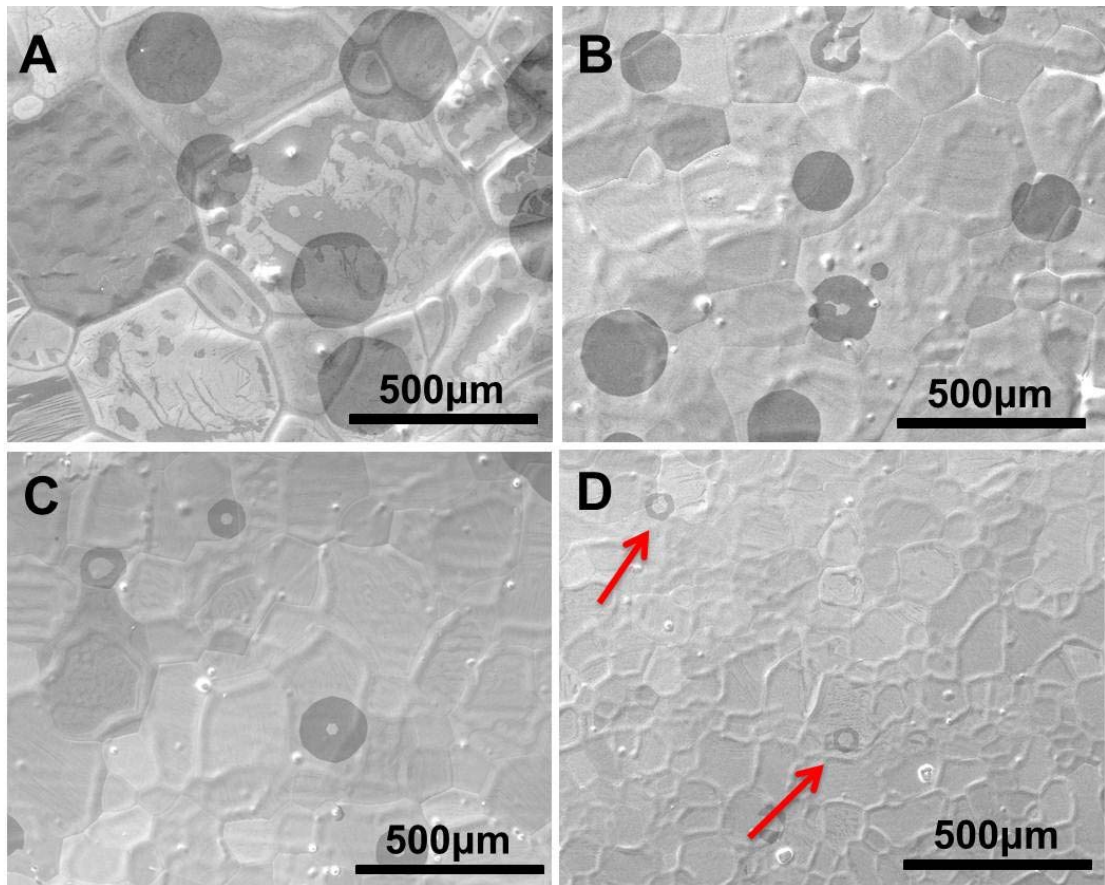


Fig. S15. Low-magnification SEM images of the graphene domains that were etched from Fig. 1B for (A) 2, (B) 4, (C) 7, and (D) 8 min in a gas flow of 700 sccm hydrogen and 3.0 sccm methane.

Table S3. Etching rates of graphene domains at different flow rate ratios of H₂/CH₄.

Temperature /°C	CH ₄ /sccm	H ₂ /sccm	H ₂ /CH ₄	Time to form a dodecagon /min	Time to form a S19 edge /min	Time to disappear /min
1040	3.3	700	212	7	12	14
1040	3.0	700	233	4	8	9

1040	3.0	720	240	2	5	5.5
1040	0	720	----	0.2	0.6	0.8

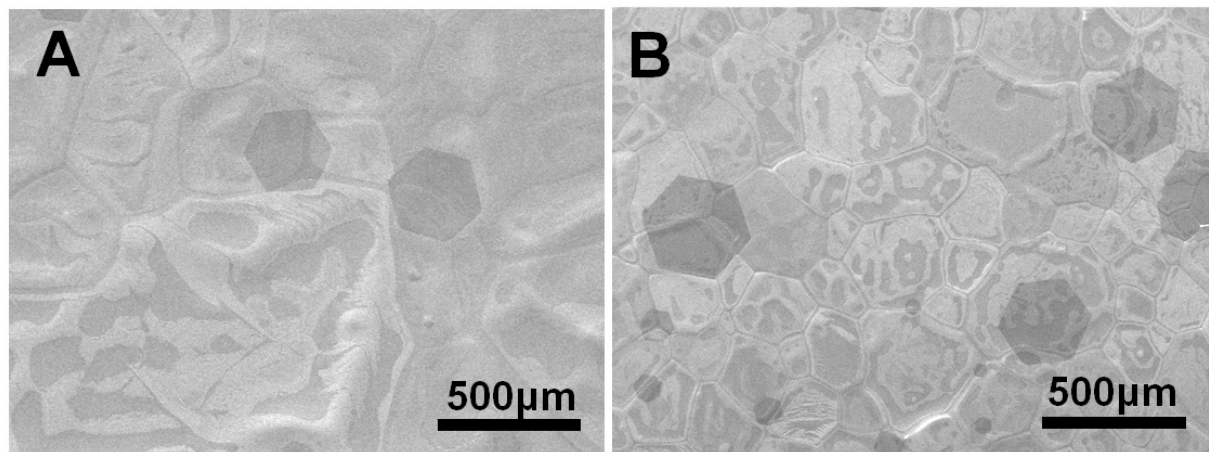


Fig. S16. Low-magnification SEM images of the single-crystal graphene domains regrown in a flow of 700 sccm hydrogen and 3.5 sccm methane from Fig. 1G in the main text with regrowth time of (A) 15 and (B) 21 min. Note that further extending regrowth time only leads to a continuous growth of the domain but without any morphology change.

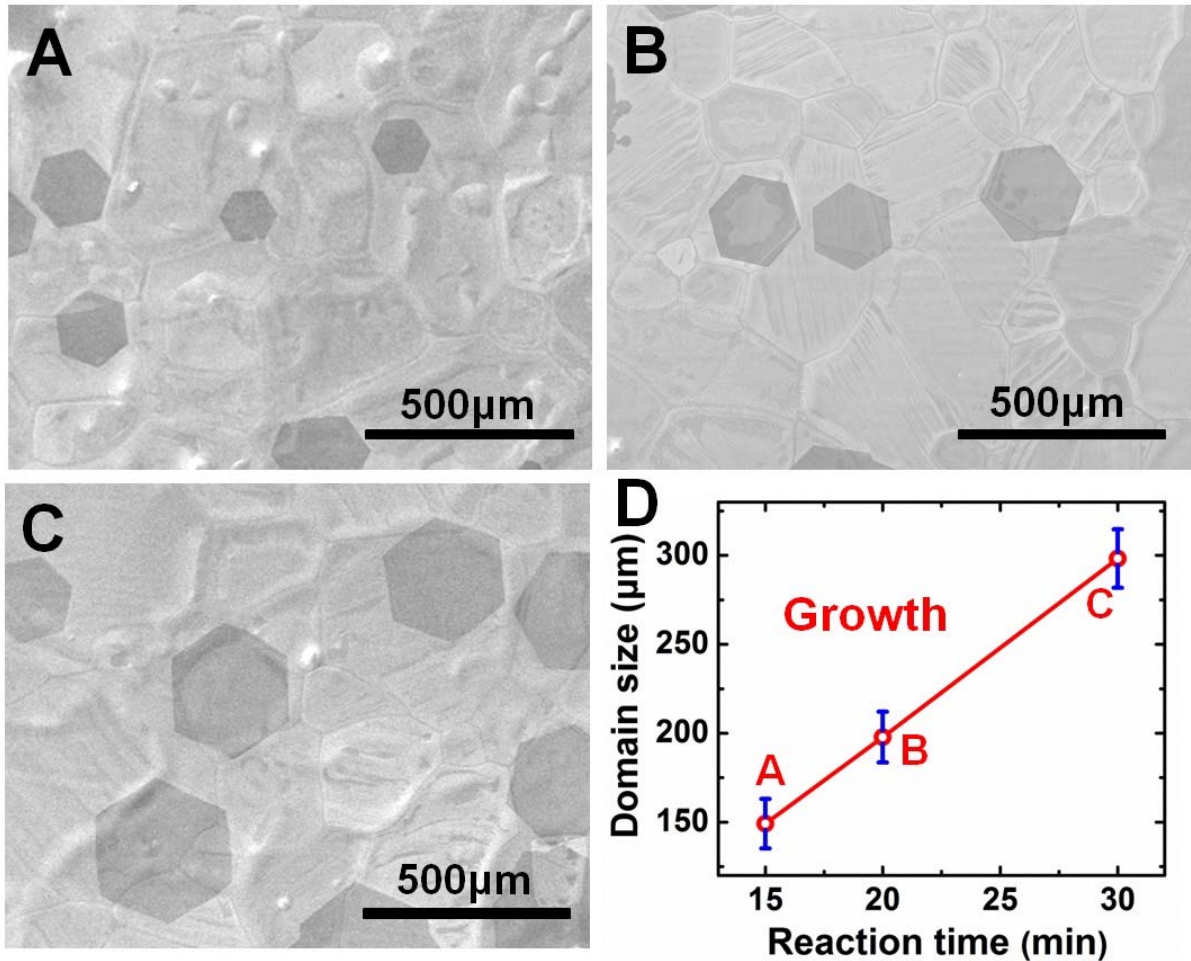


Fig. S17. (A–C) SEM images of the ZZ-edged hexagonal single-crystal graphene domains grown in a flow of 700 sccm hydrogen and 3.7 sccm methane with growth time of (A) 15, (B) 20, and (C) 30 min. (D) Size evolution of the ZZ-edged hexagonal single-crystal graphene domains with reaction time, showing a linear behavior. The red line represents fitting curve. The derived growth rate of the ZZ-edged hexagonal single-crystal graphene domains is $\sim 10 \mu\text{m}/\text{min}$, which is a little larger than the regrowth rate of ZZ-edged domain shown in Fig. 2B in the main text because of the larger methane flow rate.

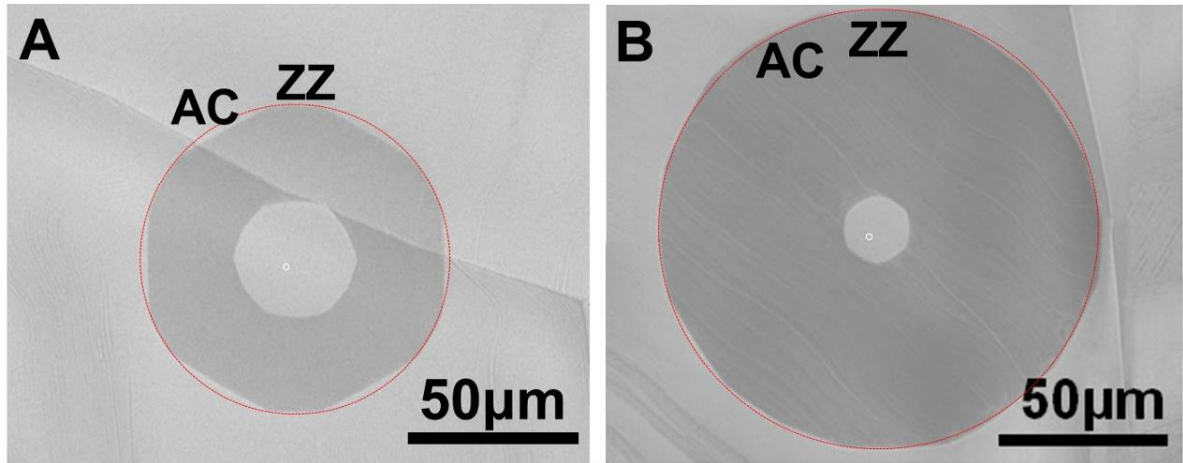


Fig. S18. SEM images of the single-crystal graphene domains regrown in a flow of 700 sccm hydrogen and 3.5 sccm methane from Fig. 1G in the main text with regrowth time of (A) 0.5 and (B) 2 min. The dot circles are used as a guide to show the difference in radial size of the ZZ and AC edges. Note that the radical size increase of the AC edges is larger than the ZZ edges within the same reaction time, indicating the faster growth rate of the AC edges than the ZZ edges.

The calculation method for the formation energies of the ZZ- and AC-nucleus

The formation energies of the ZZ-nucleus and AC-nucleus were calculated within the framework of density functional theory (DFT) as implemented in the Vienna *Ab initio* Simulation Package (VASP; refs. 7 and 8). The exchange–correlation potentials were treated by generalized gradient approximation (GGA) parameterized by Perdew, Burke, and Ernzerhof (PBE; ref. 9). The interaction between valence electrons and ion cores was described by the projected augmented wave (PAW) method (10, 11). The energy cutoff for the plane wave functions is 400 eV. The force of 0.02 eV/Å was used as the criterion of convergence in the

geometrical optimization. The graphene ribbon-metal system was modeled as a periodic slab and the lattice constant of the metal slab was selected to be same as those of graphene. The graphene ribbons with ZZ edges and AC edges were selected with three rows of carbon atoms (see Fig. 3F in the main text) and the slab consists of three metal atomic layers. The lattice length is $13.464 \text{ \AA} \times 20.938 \text{ \AA} \times 20 \text{ \AA}$ for the slab with ZZ-edge ribbon and is $17.556 \text{ \AA} \times 20.272 \text{ \AA} \times 20 \text{ \AA}$ for the one having AC-edge ribbon. The Brillouin zone was sampled by $1 \times 1 \times 1$ grid meshes for both models using the Monkhorst-Pack scheme during the calculations.

The number of kinks along an arbitrary graphene edge

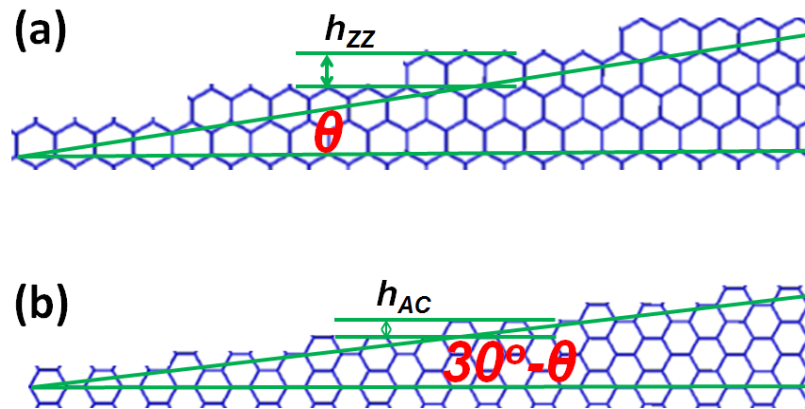


Fig. S19. The kink formation on the near the ZZ and AC edges.

As shown in Fig. S19a, for an arbitrary edge that is characterized by the slanted angle θ from the zigzag edge, the height of such a zigzag kink is

$$h_{ZZ} = 1.5a, \quad (1)$$

where $a = 0.142 \text{ nm}$ is the C-C bond length in graphene lattice. Thus the number of kinks on an edge whose length is l is

$$N_{ZZ} = l * \sin(\theta)/h_{ZZ}, \quad (2)$$

and the concentration of zigzag kinks is

$$c_{ZZ} = N_{ZZ}/l = \sin(\theta)/h_{ZZ}. \quad (3)$$

Similarly, if we take an armchair edge as a smooth edge, armchair kinks may appear on the edge that has a slanted angle of $30^\circ - \theta$ from the armchair edge. The height of an armchair kink is

$$h_{AC} = 1/2\sqrt{3} a, \quad (4)$$

which is shorter than that of the zigzag edge. Thus the concentration of armchair kinks on the edge is

$$c_{AC} = \sin(30^\circ - \theta)/h_{AC}. \quad (5)$$

We can see that there are two options to calculate the number of kinks on an arbitrary edge.

Mathematically, which formula should be used is arbitrary. For carbon nanotube growth from the catalyst particle, Eq. (3) is used because the nucleation of a near hexagon from the armchair edge has nearly zero formation energy. While, for the graphene CVD growth, nucleation of a new hexagon from either zigzag or armchair edge has significantly large formation energy, so it is natural to choose the armchair edge as the reference for the edges with slanted angle near 30° and choose zigzag edge as the reference for edges with slanted angle near 0° . For those edges with a slanted angle away from 0° or 30° , we choose the least number of two types of kinks on the edge in order to avoid the formation of two adjacent kinks staying together. That is

$$\begin{aligned} c_K &= \min(c_{ZZ}, c_{AC}) = \sin(\theta)/h_{ZZ}, \quad \text{for } 0^\circ < \theta < 19.107^\circ \\ &= \sin(30^\circ - \theta)/h_{AC}, \quad \text{for } 19.107^\circ < \theta < 30^\circ \end{aligned} \quad (6)$$

where $\theta = 19.107^\circ$ is the slanted angle when $c_{AC} = c_{ZZ}$, which corresponds the slanted angle of the edge with the maximum number of kinks. Considering that $\sin(\theta) \sim \theta$ for small slanted angles, Eq. (6) can be rewritten as:

$$c_K = \begin{cases} \theta/h_{ZZ}, & \text{for } 0^\circ < \theta < 19.107^\circ \\ (30^\circ - \theta)/h_{AC}, & \text{for } 19.107^\circ < \theta < 30^\circ \end{cases} \quad (s7)$$

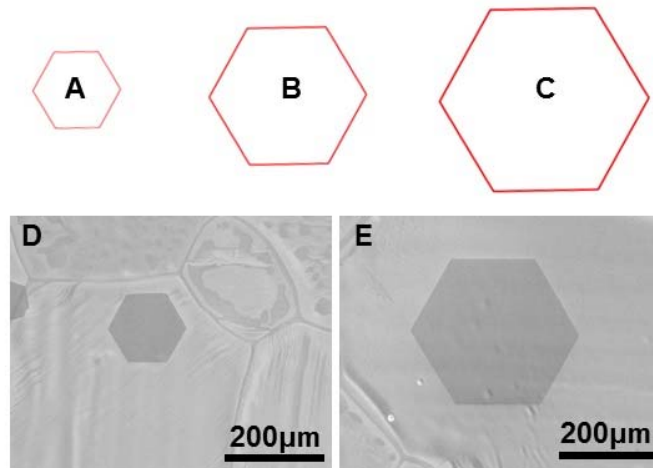


Fig. S20. (A–C) Illustrations of graphene growth obtained based on the edge structure dependent growth behavior and the theory of kinetic Wulff construction. (D and E) SEM images of the hexagonal graphene domains obtained with different growth time, corresponding to those shown in Fig. 1A and B in the main text. Kinetically, the edges that grow faster become smaller and smaller during CVD growth and eventually only those edges that grow most slowly, i.e., the ZZ edges, survive and remain no change with further extending growth time. Note that the simulated structural evolution is in good agreement with the experimental observations.

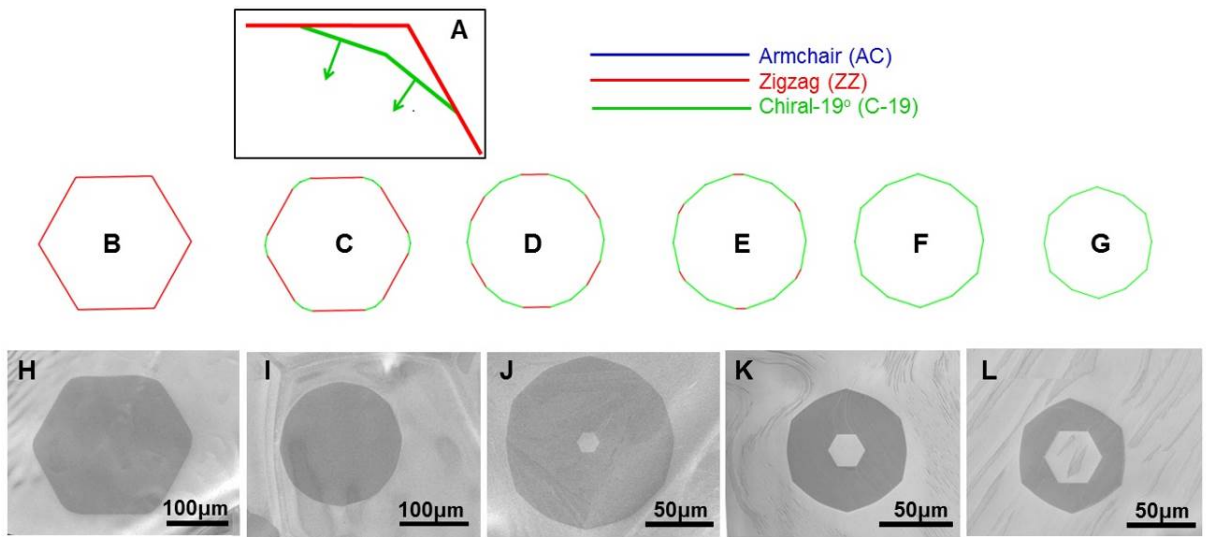


Fig. S21. (A) Illustration of the appearance of quick etching edges from the vortexes of the ZZ edged graphene islands. (B–G) Descriptions of the graphene etching process obtained based on the edge structure dependent etching behavior and the theory of kinetic Wulff construction. (H–L) SEM images of an etched graphene domain with different etching time, corresponding to those shown in Fig. 1C–G in the main text. Etching is a process of shrinkage and thus the fast etching edges would dominate the process. First, the fast etching edges appear on each vortex of the ZZ edges and gradually become the dominating component of the circumference by fast etching. Once all ZZ components disappear, the domain becomes a dodecagon with twelve equivalent edges and remains no change in the morphology and edge structure during further etching. Note that the simulated structural evolution is in agreement with the experimental observations.

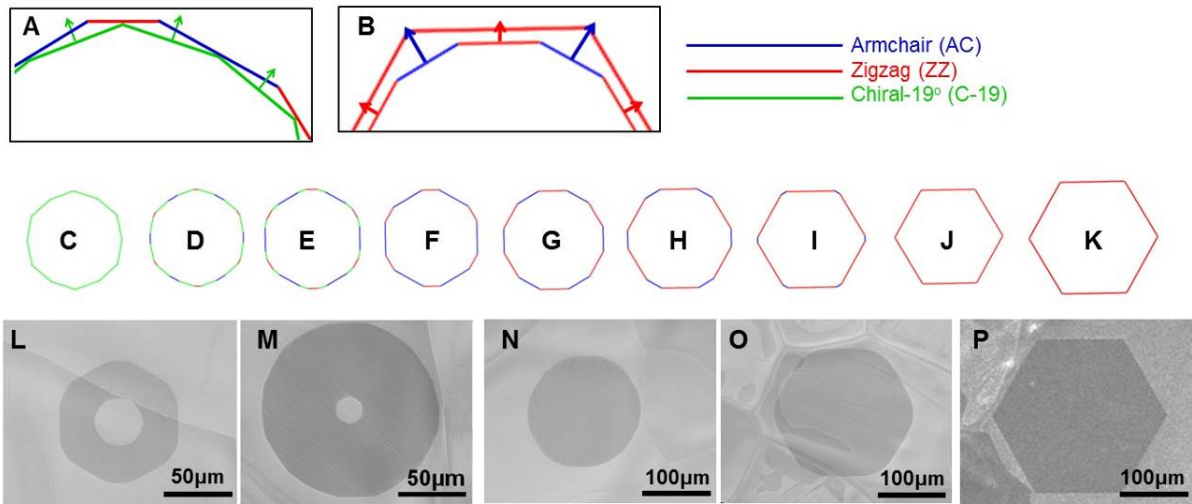


Fig. S22. (A) Illustration of the emergence of the slow growing AC (Blue) and ZZ (Red) edges during the fast propagation of the S19 edge (green). (B) Illustration of the process from ZZ and AC alternatively to the whole ZZ edges. (C–K) Descriptions of the regrowth process of a graphene domain obtained based on the edge-structure dependent growth behavior and the theory of kinetic Wulff construction. (L–P) SEM images of the regrown graphene domains with different regrowth time, corresponding to those shown in Fig. 1H–L in the main text. Regrowth is a process of size expansion and thus the slowest growing edge (ZZ edge) would dominate the process eventually. For regrowth starting with a dodecagon (C), the very quick growth or propagation of the twelve slanted edges leads to the formation of AC and ZZ edges from the twelve vortexes (C→D→E→F). And the AC edges are greater than the ZZ edges because the S19 edge is closer to the AC (~11° away) than the ZZ (~19° away) edge. After the disappearance of the S19 edge, the competition between AC and ZZ edges dominates the regrowth process. The relative fast growing AC edges gradually disappear and the ZZ edges keep increase (F→G→H→I→J). Eventually, all of the circumference becomes ZZ edges and remains no

change during further growth (J→K). Note that the simulated structural evolution is in perfect agreement with the experimental observations.

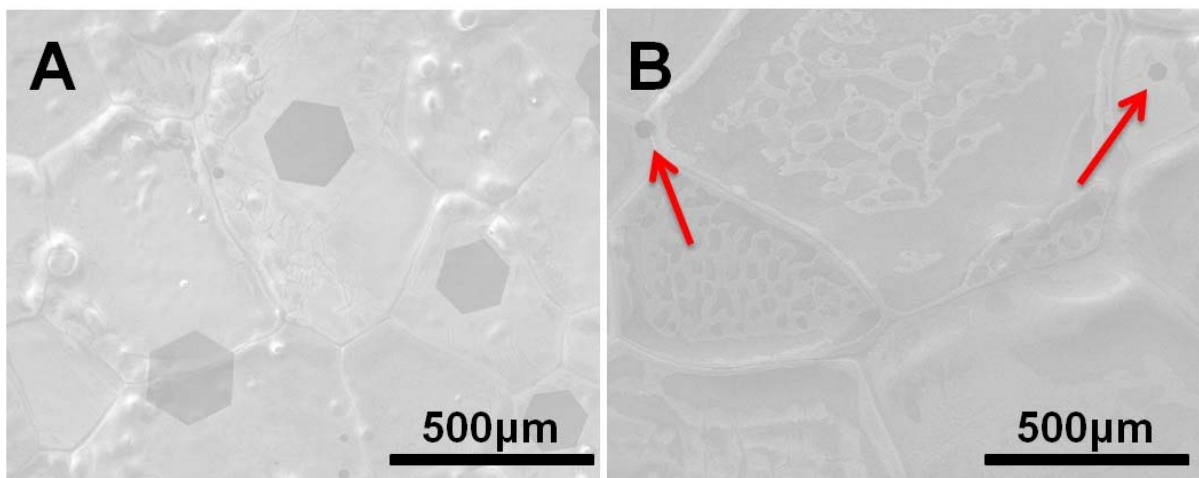


Fig. S23. (A) Low-magnification SEM image of the regrown hexagonal single-crystal graphene domains in a gas flow of 700 sccm hydrogen and 3.5 sccm methane for 7 min from Fig. 1G in the main text. (B) Low-magnification SEM image of the near hexagonal single-crystal graphene domains (denoted by red arrows) obtained by etching the graphene domains in a gas flow of 700 sccm hydrogen and 3.3 sccm methane for 8 min from A.

References

1. You YM, Ni ZH, Yu T, Shen ZX (2008) Edge chirality determination of graphene by Raman spectroscopy. *Appl Phys Lett* 93(16):163112.
2. Cong CX, Yu T, Wang HM (2010) Raman study on the G mode of graphene for determination of edge orientation. *ACS Nano* 4(6):3175-3180.

3. Casiraghi C, et al (2009) Raman spectroscopy of graphene edges. *Nano Lett* 9(4):1433-1441.
4. Krauss B, et al (2010) Raman scattering at pure graphene zigzag edges. *Nano Lett* 10(11):4544-4548.
5. Malard LM, Pimenta MA, Dresselhaus G, Dresselhaus MS (2009) Raman spectroscopy in graphene. *Phys Rep* 473(5-6):51-87.
6. Yu Q, et al. (2011) Control and characterization of individual grains and grain boundaries in graphene grown by chemical vapor deposition. *Nat Mater* 10(6):443-449.
7. Kresse G, Hafner J (1993) Ab initio molecular dynamics for open-shell transition metals. *Phys Rev B* 48(17):13115-13118.
8. Kresse G, Furthmüller J (1996) Efficiency of ab initio total energy calculations for metals and semiconductors using a plane-wave basis set. *Comput Mater Sci* 6(1):15-50.
9. Perdew JP, Burke K, Ernzerhof M (1996) Generalized gradient approximation made simple. *Phys Rev Lett* 77(18):3865-3868.
10. Blochl PE (1994) Projector augmented-wave method. *Phys Rev B* 50(24):17953-17979.
11. Kresse G, Joubert D (1999) From ultrasoft pseudopotentials to the projector augmented-wave method. *Phys Rev B* 59(3):1758-1775.